SUBSURFACE CONDUCTIVE ISOLATION OF

REFRACTION CORRELATIVE MAGNETIC SIGNALS (SCIRCMS)

A Dissertation

by

ERIC STEPHENSON ERCK

Submitted to the Office of Graduate Studies of
Texas A&M University
in partial fulfillment of the requirements for the degree of

DOCTOR OF PHILOSOPHY

August 2004

Major Subject: Geophysics

SUBSURFACE CONDUCTIVE ISOLATION OF

REFRACTION CORRELATIVE MAGNETIC SIGNALS (SCIRCMS)

A Dissertation

by

ERIC STEPHENSON ERCK

Submitted to Texas A&M University
in partial fulfillment of the requirements
for the degree of

DOCTOR OF PHILOSOPHY

Approved as to style and content by:

William W. Sager (Co-Chair of Committee)	Mark E. Everett (Co-Chair of Committee)
David. V. Wiltschko (Member)	Robert L. Lytton (Member)
Richard L. Carlson (Head of Department)	

August 2004

Major Subject: Geophysics

ABSTRACT

Subsurface Conductive Isolation of Refraction Correlative Magnetic

Signals (SCIRCMS). (August 2004)

Eric Stephenson Erck, B.S., Purdue University;

M.S., Iowa State University

Co-Chairs of Advisory Committee: Dr. William Sager
Dr. Mark Everett

Isolation of terrestrially-observed magnetic signals by restoring their diffusive loss due to subsurface electrical conductivity sufficiently correlates these signals with those derived from the Alfven ionospheric electron movement of refraction variation. Temporary magnetic observatories were established on a conductive sedimentary basin (with a sampling interval of 5 s) and on a resistive large igneous intrusion (with a sampling interval of 10 s). Conventional modeling techniques estimate and remove the effects of the magnetometer, geomagnetic diurnal changes, whorls (solar quiet current vortices), and some bays from the acquired signals. Conventional one-dimensional skin depth modeling estimates the diffusive attenuation. The residual magnetic signal and the diffusive filter (as applied to the topography) become quantities in the linear system estimation of the geoelectric subsurface. Angular frequency domain least squares solution of the equations yields an isolated magnetic anomaly spectrum. Interpretive refinement, by selection of the zero or near zero

curvature onset of either the spectrum's real or imaginary component, critically prepares the signal solution for correlation to a pseudomagnetic anomaly signal. This is an independently-derived sequence of anomalous values derived from Global Positioning System (GPS) refracted ranges. Detailed application of the Biot-Savart law provides independent anomaly signals to which the magnetic anomalies correlations show great correlation improvement by the isolation. These correlation improvements are from 2% to 83% and 9% to 91% for the sedimentary basin and from 2% to 96% and 24% to 78% for the igneous intrusion.

ACKNOWLEDGMENTS

Many individuals, both in Texas A&M University and its Department of Geology and Geophysics and outside it, are deserving of thanks. Especially, but not exclusively, they include Dr. Davis A. Fahlquist for his preliminary endorsement of this research, particularly at the end of his career. Dr. William W. Sager re-informed me of the many sources of geomagnetic variations with time. Dr. Mark E. Everett is to credit for providing me with a better electromagnetic perspective and his sustained review of this work's progress. For his GPS and structural geology expertise, one must surely mention Dr. David V. Wiltschko and Dr. Robert L. Lytton for his consultation concerning cultural factors related to electromagnetic wave earth impingement including that applied to GPS use.

In no way can Mr. Gerald J. Creager be neglected for his notification of possible GPS multipath problems. Similarly, Mr. Carl J. Pierce must be thanked for his introductory help with G-858 magnetometry. The same extends to Mr. Robert A. Renzetti and Mr. Steve Tran for their departmental hardware assistance. Finally, the Texas A&M University Department of Geology and Geophysics office staff needs to be thanked for their presentation assistance.

TABLE OF CONTENTS

LIST OF FIGURES

FIGURE Page

FIGURE Page

FIGURE Page

1. INTRODUCTION

The complexity of the earth's natural magnetic field is a measure of our understanding of it. For centuries, the direction of the field has been used as an approximation for North. This gave rise to a dipole mechanism for the field (Figure 1). Now we know that this is only a generalization of a dynamo model of approximately eastward spinning ions in the outer core. This does not, however, explain the common oscillations in the magnitude of the geomagnetic field which range in period from about one second to about 24 hours.

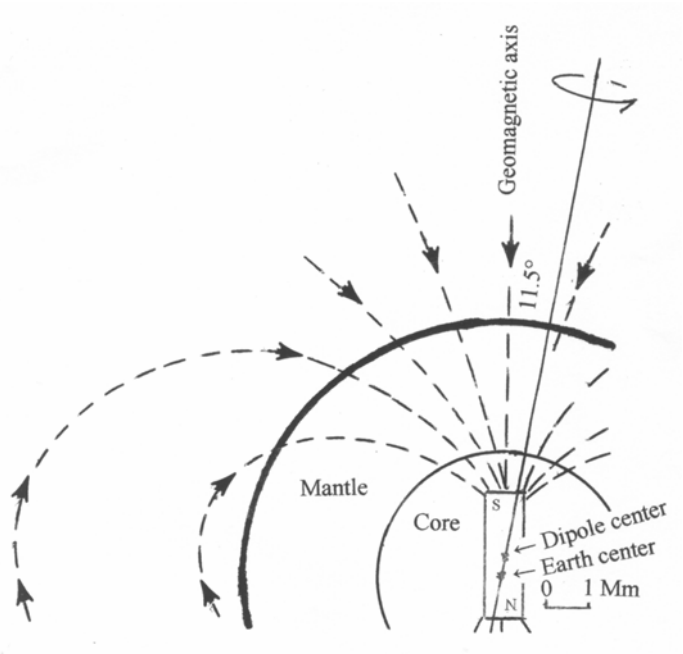

Figure 1. Simple dipole model for a magnetic earth.

This dissertation follows the style and format of *Journal of Geophysical Research.*

Around the year 1960, a second source of field-affecting ions was discovered: random solar wind which sometimes flares into high-amplitude geomagnetic storms. (Figure 2.) The solar wind interacts with the earth's ionosphere in two major ways (Figure 3). The first and more systematic way is the Alfven wave pulse [*McPherron*, 2002]. This is a group of ions quickly (about 0.59 MHz) gyrating around main earth magnetic flux lines. Alfven electron movement is a variety of ultra low frequency (ULF) waves by its frequency and part of the magnetohydrodynamic process because the pulses move along main earth magnetic field lines in the magnetosphere and the ionosphere. The other way solar wind interacts with the ionosphere is the creation of vortices of ions rotating mostly horizontally [*Spaulding*, 1995]. Both of these create anomaly signals which can be sensed on the topography.

The present status of how the solid earth affects the magnetosphere and the ionosphere has come from artificial satellite data. Magnetic satellites (MAGSAT) and the Global Positioning System (GPS) and its associated receivers have significantly, albeit to a low spatial resolution, contributed to our magnetospheric and ionospheric knowledge. *Bassiri and Hajj* [1993] have been concerned about their uncertainties in the ionospheric magnetic field calculated by a dipole model only. The reason for this is that both accurate magnitude and direction of this field are required for index of refraction (refractive index or refractivity) calculations. Since 1993, ionospheric density mapping by satellite-to-satellite range occultation has advanced using low earth orbiting (LEO) satellites [*Hajj and Romans*, 1996]. As for

seismic velocities, global models have evolved for ionospheric electron density only.

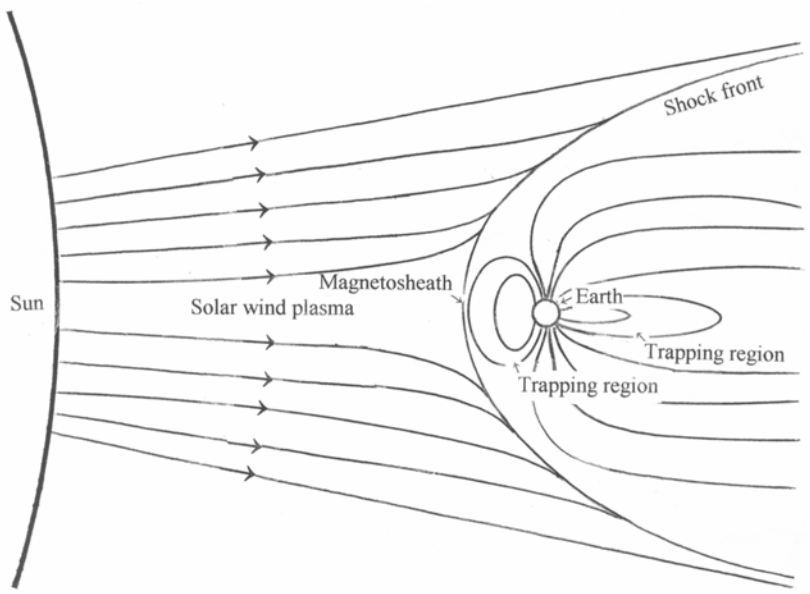

Figure 2. Geomagnetic dipole in the solar wind.

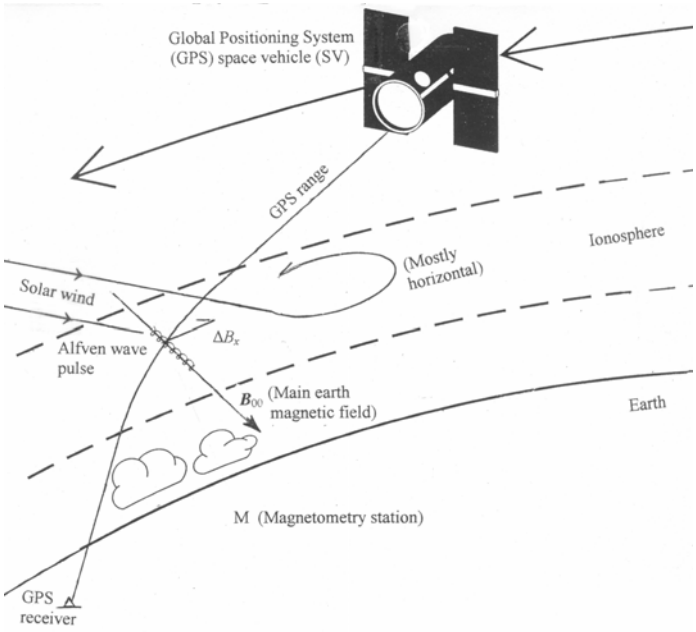

Figure 3. Interaction of solar wind, the ionosphere, the geomagnetic field, and a GPS range. (Reprinted with permission from *Differential GPS Explained* by *J. Hurn*, 1993, Trimble Navigation, Sunnyvale, CA, 1993, Trimble Navigation.)

Afraimovich [2000] monitored this quantity using GPS. *McPherron* [2002] attributes magnetic field changes not only to solar wind conditions, but also to solid earth conductivities. Isolation of terrestrially-observed magnetic signals by restoring their diffusive loss to subsurface conductivity can correlate these signals with those from refraction variation resulting from Alfven ionospheric electron movement.

The means by which this hypothesis is realized is summarized in Figure 4.

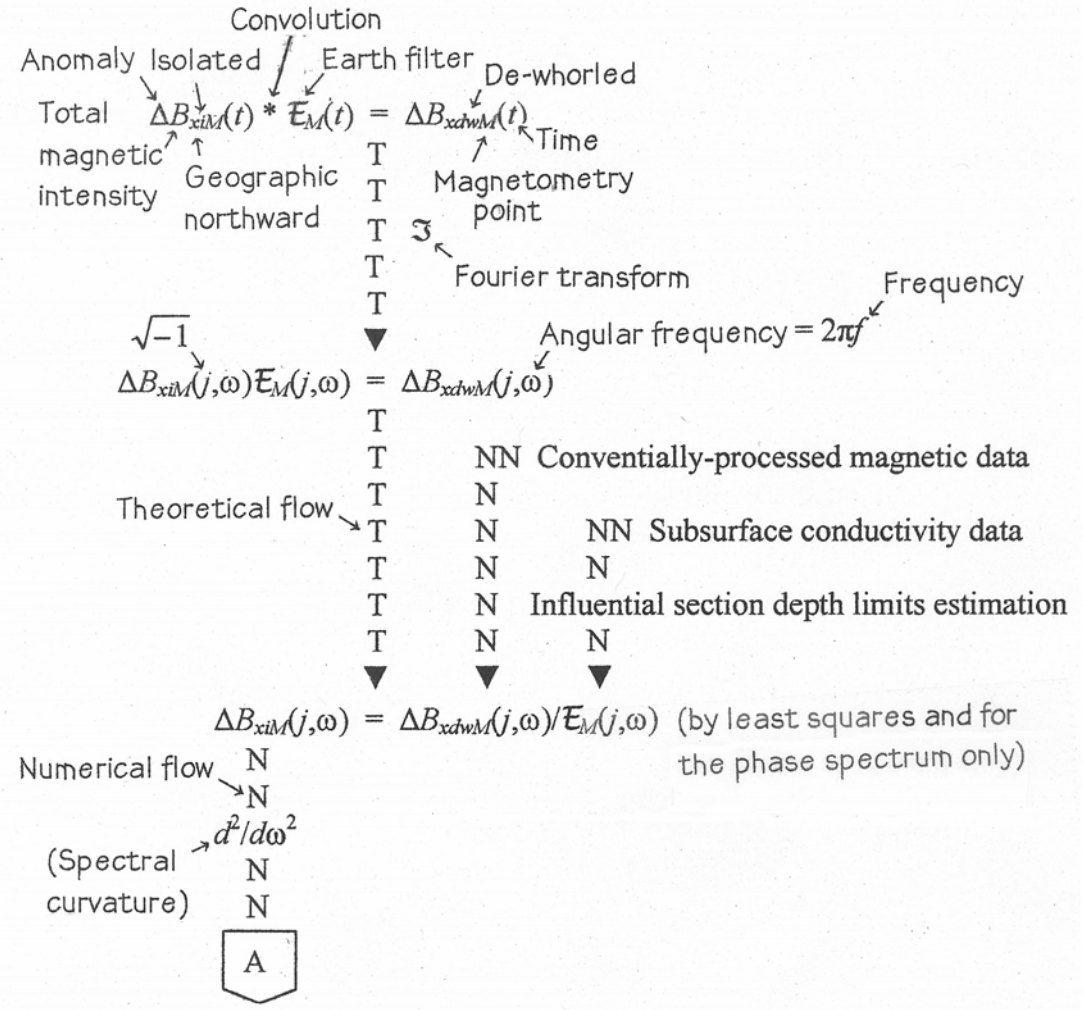

Figure 4. Schematic theoretical and numerical flowchart with symbols explained.

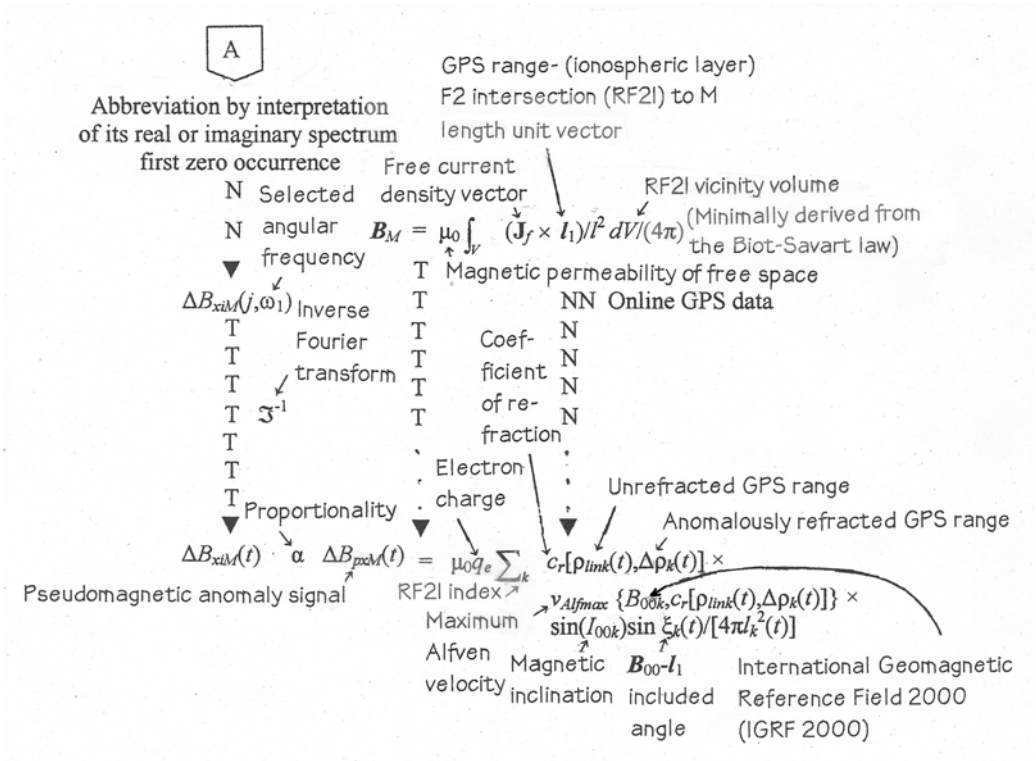

Figure 4. Continued.

Acquisition, processing, and correlation of static terrestrial magnetic observations to Alfven refractivity models derived from GPS range data. The observation sites selected were over a sedimentary basin (Butler Bayou in southeast Texas) and a large crystalline intrusion (Enchanted Rock in central Texas). An electromagnetic linear system was assumed to describe the convolution of the unknown isolated magnetic signal with the earth filter (constructed from known subsurface conductivities, the observational duration, and sample interval) to produce the observed magnetic signal.

In addition to being highpass filtered, this signal lacks the low frequency components that diffusively penetrate into the earth. With this signal stationary, Fourier transform turned the convolution in the time domain into multiplication in the angular frequency domain. For simplicity, Figure 4 expresses what is actually least squares inversion for the phase spectra as division, the quotient of which is the spectrum of the magnetic field caused by all ionospheric electron movement. The Alfven isolation process then begins by taking the curvature (second angular frequency derivative) and selecting its lowest frequency zero or near zero. Inverse Fourier transformation of a singularity of any positive ordinate at this frequency, coupled with the corresponding phase angle solution, produces the isolated signal to be correlated. An equation, minimally derived from the Biot-Savart law, and GPS range data combine to form a signal with which the isolated signal was correlated. This provided the system by which differentially-refracted electron density movement could be sensed by a magnetometer. The Biot-Savart derivation theoretically continued to include observable quantities (GPS ranges) which varied with ionospheric electron movement.

The results from both study stations show striking improvements in isolated-refraction derived signal correlation upon this removal of the effects of the subsurface. This greatly improves our observation and analysis of the magnetic field vector that is anomalous by ionospheric plasma only. The importance extends to more applied aeronomy as it adds to the *Afraimovich* [2000] capability of quantifying

ionospheric electron content. The combination provides the two time varying quantities by which the very useful (for radio science and radio engineering design) index of refraction is determined [*Bassiri and Hajj*, 1993]. While analytically complicated, the model for this describes the amount, magnetic intensity, and direction by which highly gyrating densities of electrons move along a flux line that has some spatial relationship with an artificial electromagnetic Poynting vector to change its direction.

2. THEORY AND METHODS

2.1. Surface Magnetic Data Field Acquisition and Its Conventional Processing

The terrestrially-observed magnetic data are in the form of an evenly sampled signal over time. A Geometrics G-858 (cesium vapor) portable magnetometer was used in its base station mode and with the sensor kept most sensitive to the northward magnetic component. This instrument configuration can measure this component of all (ULF) pulsations in which the Alfven are included. Two main criteria regulate the field acquisition of the signals.

The first of these are the temporal criteria. To most easily make the observed signals stationary by processing, the survey must be designed to minimize whorls [*Telford et al*., 1982] (solar quiet current vortices) and most bays [*Sheriff*, 1991]. Whorls are systematic and continental-sized horizontal vortices in the ionosphere. They are independent of random solar wind received directly during daylight. Bays are also horizontal vortices, but are smaller, more random, and include the daylight effect. They may also include the effect of polar substorms which produce a several hour equatorward growth and recovery of a polar auroral zone. *Sheriff* [1991] offers a semi-qualitative global frequency spectrum of magnetic field strength. Whorls have been added to this in Figure 5 as have *McPherron* [2002] (ULF) pulsations, which include electron movement of both the pulsation constituent types: vortex and Alfven. Spectral dimensions for the two study stations have been described in this

figure. The lower limits of these are the reciprocal of the magnetic survey durations.

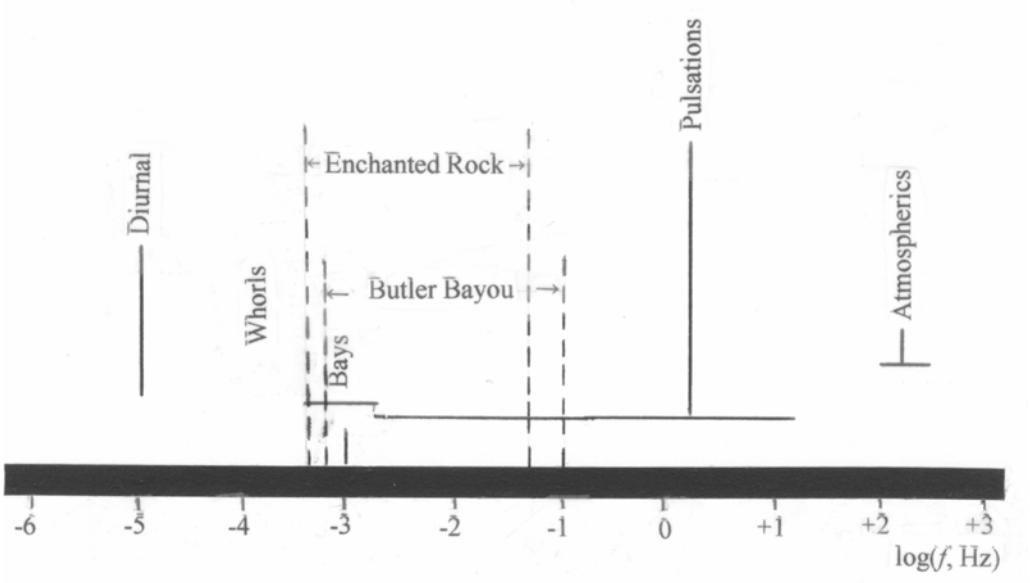

Figure 5. Natural magnetic amplitude semi-quantitative spectrum with each study station duration frequency and Nyquist frequency limits. They differ because each station's sample interval and observation time length differ. (Reprinted with permission from *Encyclopedic Dictionary* of *Exploration Geophysics* by *R. E. Sheriff,* 1991, Society of Exploration Geophysics, Tulsa, OK, 1991, Society of Exploration Geophysicists.)

The speed [*Seeber*, 1993] of the GPS space vehicles (SVs) (satellites) mostly controls this since there is only so much time that continuous GPS range-ionosphere intersections can pass nearby the magnetometry station. This proximity strengthens the magnetic signal that is to be correlated with that derived from the refracted GPS GPS ranges. The upper limits of the study station dimensions are the magnetometry Nyquist frequencies for the 5 s (Butler Bayou) and 10 s (Enchanted Rock)

magnetometry sample intervals. The lower limits indicate observation times of 21 minutes, 20 seconds for Butler Bayou and 42 minutes, 40 seconds for Enchanted Rock. Since Figure 5 is a global average, it provides data for the survey parameters equally for anywhere in the world and under any geomagnetic conditions. (Geomagnetic storms are of too low frequency to interfere with Alfven pulsations.)

Spatial criteria were also considered in the field data acquisition. Stations were chosen to be reasonably removed from cultural magnetic noise sources, the effects of which lasted near the observation durations [*Breiner*, 1973]. These sources needed not be absent, just relatively static with respect to the durations. Significant celestial hemisphere visibility [*Vozoff*, 1972] was also considered in station site selections. The priority was for unobstructed views of the majority of SVs at any given moment. The station locations are accurate to about 1 m.

Figure 6 shows the data processing. Its left (connected to A) column relates to the magnetometer. The instrument memory contains sequences of measurements at stations M going backwards in time [*Geometrics*, 1995], so they were reversed in the "Signal time reversal" process. Reformatting followed to reject unneeded bytes such as those containing the date.

A sequence of more ordinary magnetic data processing steps then prepared the data for subsurface conductive filtering. These first included selection of time intervals ("Interval selection") which contained a variety of frequencies and corresponding relative amplitudes. Since the diurnal, whorl, and bay effects are substantially outside Figure 2 limits for the two study stations, they were modeled as polynomials of degree one and degree two. The degree one polynomial accounted for the (fundamentally non-equivalent) diurnal and whorl effects. The second degree polynomial mostly removed the effects of the bays; as this name suggests, these anomalies over time look like a map of a bay, which looks parabolic. The third degree sum of these polynomials, including a 30% approximation [*Everett*, 2002] of the signal lost to the subsurface in this frequency band, was removed for a de-whorled magnetic intensity anomaly ΔB_{dwM} of time t. These are the "(Linear) diurnal effect modeling and removal" and the "(Quadratic) diurnal effect modeling and removal" processes. The effects of them are shown in Section 3.

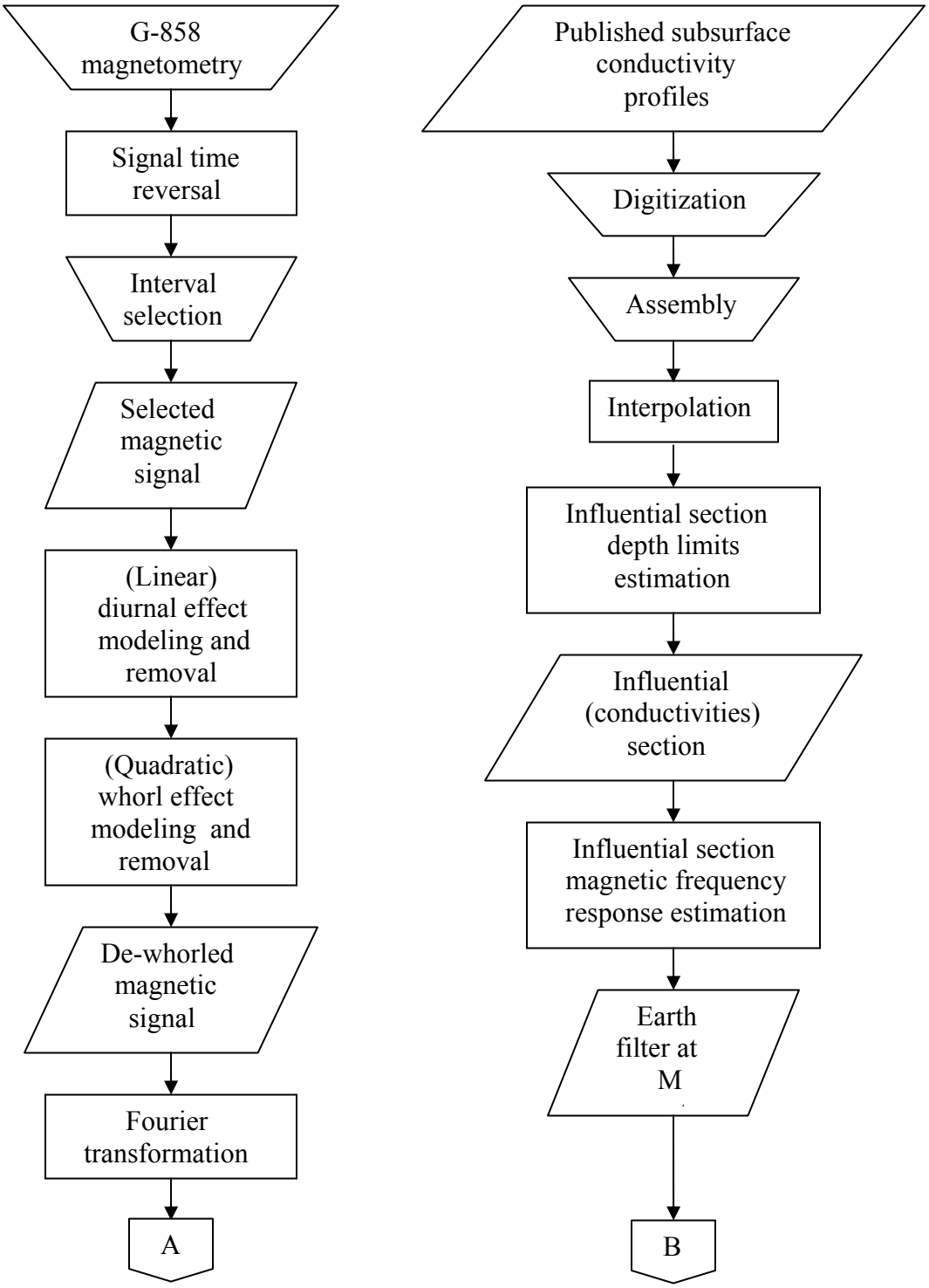

Figure 6. Data processing flowchart (numerical flow detail).

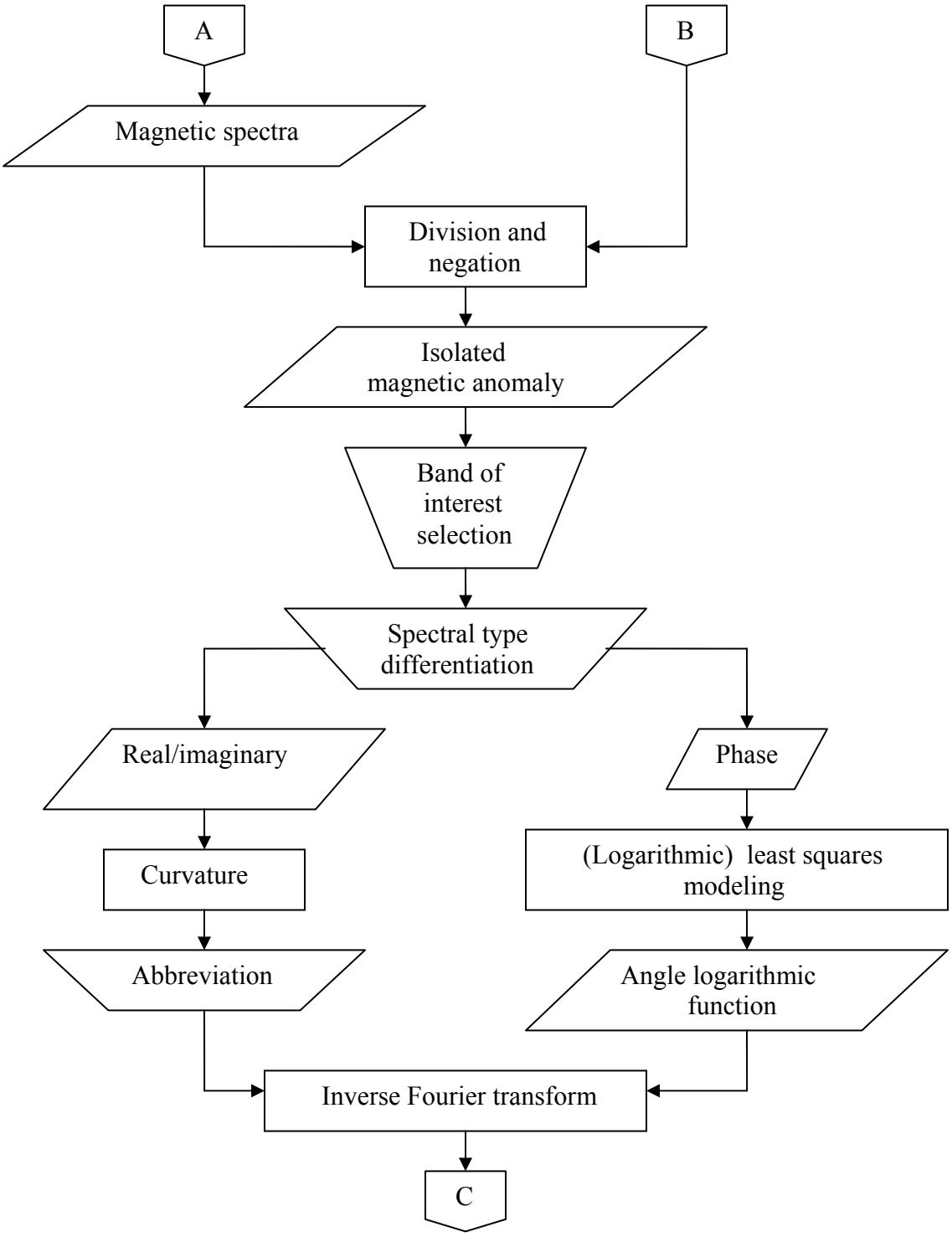

Figure 6. Continued.

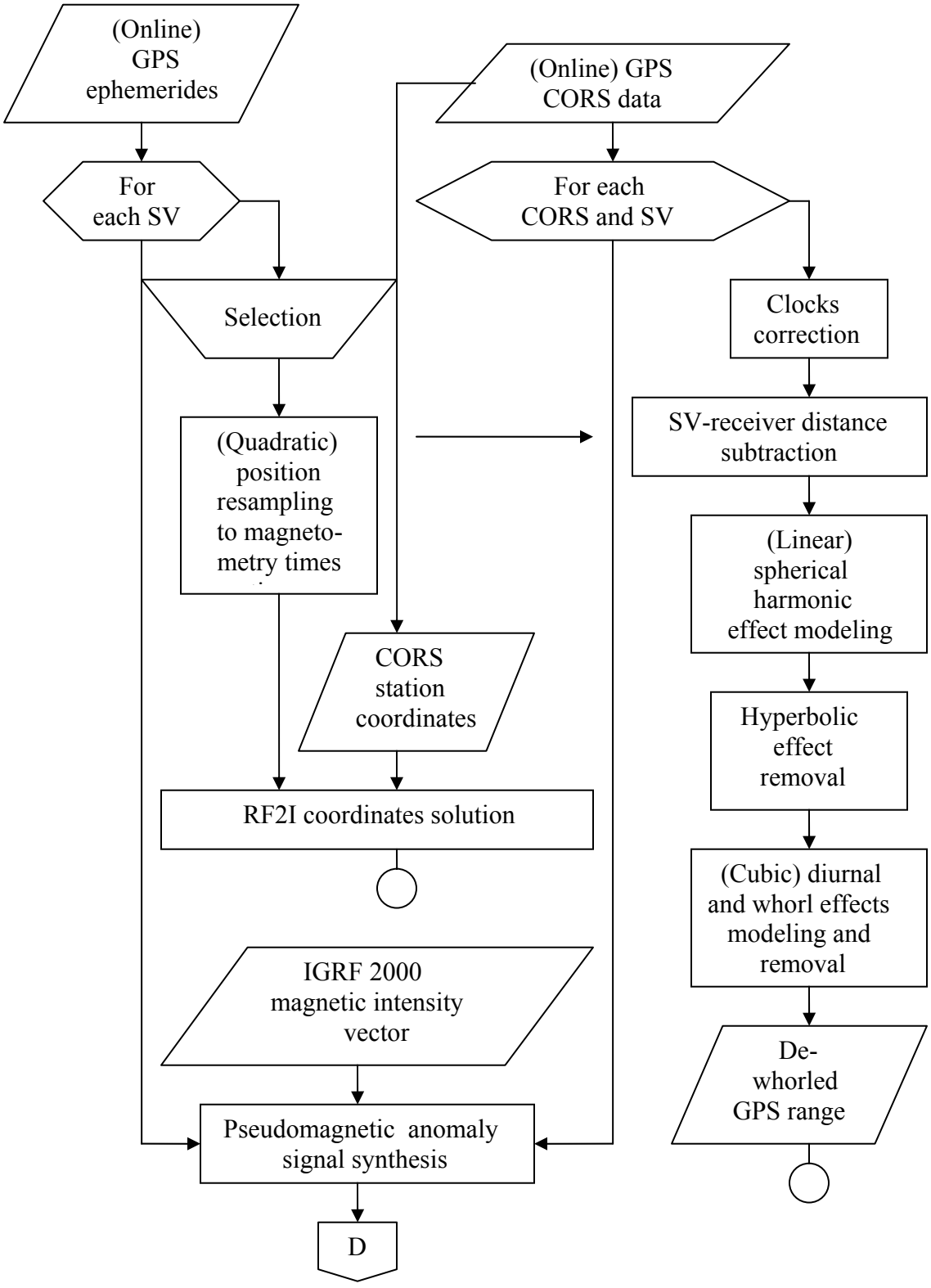

Figure 6. Continued.

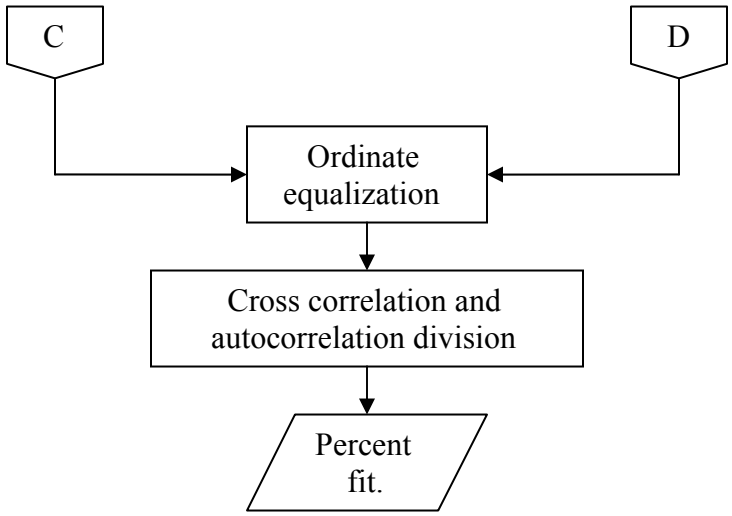

Figure 6. Continued

$\Delta B_{dwM}(t)$ became complex $\Delta B_{dwM}(j,\omega)$ after the application of a fast Fourier transform algorithm [*Robinson*, 1983]. The column connected to B involved digitization with a planimeter-type digitizer of the conductivity profiles in Section 3. The influential section processes are described in the next Section.

2.2. Subsurface Conductive Filtering

Unlike many geophysical methods, SCIRCMS solutions describe volume at or above the topography and not subsurface scalar, tensor, or structural quantities. Neither do SCIRCMS solutions provide data to constrain inversions for subsurface interpretation. Globally, the input subsurface conductivity data are represented by *Constable* [1993] in Figure 7. This graph shows the general

increase of mantle conductivity with depth. It is significant and noteworthy because it relates global magnetic observatory obtained conductivities with those obtained from a considerably different method: the diamond anvil thermal-conductivity behavior of deep mantle olivine varieties. (Specifically these

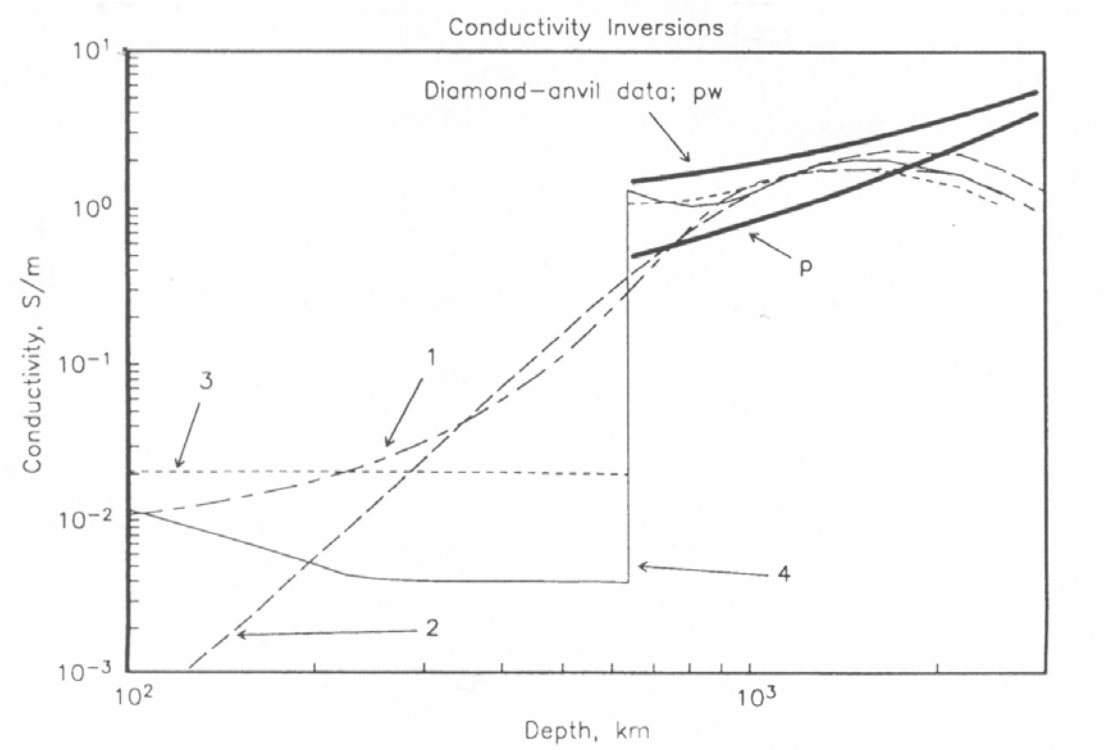

Figure 7. Global mantle conductivity functions as compiled by *Constable* [1993] with numbers labeling geophysically-derived functions and letters labeling petrologically-derived functions. *Constable* [1993] also provides the very lengthy and very involved statistical keys to the numerical and letter labeling. (Reprinted with permission from "Constraints on Mantle Electrical Conductivity from Field and Laboratory Measurements" by *S. Constable,* 1993, *J. Geomag. Geoelectr., 45*, 707-728, 1993, The Society of Geomagnetism and Earth, Planetary and Space Sciences.)

varieties are perovskite and perovskite plus wustite, both with 11% iron.) [*Constable*,

1993]. The global magnetic observatory data are horizontal and vertical intensity components. The potential from which these components are taken is ascribed to a zonal spherical harmonic model in geomagnetic spherical coordinates. At any degree of the model, the ratio of internal coefficients to external coefficients at any frequency is proportional to conductivity at depth; lower frequencies yield deeper conductivity data. As can be seen from especially the shallow portion, there is much variability in the global conductivity model. This is indicative of substantial geographic variability for mantle conductivities.

Lizarralde et al. [1995] and *Keller and Fritschknect* [1966] provide data to more regionally refine the *Constable* conductivity model while maintaining the general increase in mantle conductivity with depth. While *Lizarralde et al.* featured a method to obtain low frequency magnetotelluric soundings to provide mantle conductivity data under oceanic crust, they included data from similar studies over sedimentary extensional and granitic rocks. These data provide estimation for Butler Bayou and Enchanted Rock mantle conductivity profiles. *Keller and Fritschknect* provide, from laboratory measurements, conductivity data for the sedimentary formations beneath the Butler Bayou study station. The “Digitization” and “Assembly” (from different sources) processes of the data form the appropriate conductivity models for field study stations. Profiles were linearly interpolated (the “Interpolation” process) to form the one

dimensional conductivity models from which subsurface magnetic intensity diffusion can be estimated.

From *Vozoff* [1972], horizontally-polarized plane electromagnetic waves (frequency < 1 Hz) incident on topography bounding a semi-infinite volume of isotropic and constant conductivity σ attenuate to 1/*e* times their impingement amplitude at a skin depth

$$z = [2/(\sigma\mu\omega)]^{1/2} \tag{1}$$

with angular frequency ω and magnetic permeability (considered constant) $\mu = \mu_0 = 4\pi \times 10^{-7}$, the magnetic permeability of free space. (The semi-infinite volume is non-magnetic.) This volume passes the longer wavelengths (lower frequencies and higher periods) of the magnetic energy. The function for the minimum period present at *z* then is

$$T_{min}(z) = \pi\mu z^2\sigma. \tag{2}$$

More realistically, the one dimensional model includes known but variable σ(*z*). Accommodation (now considering variable conductivity) of this function for minimum period T_{minvc} requires taking the vertical skin depth derivative

$$\frac{d}{dz}\ T_{minvc}(z) = \pi\mu \frac{d}{dz}[z^2\sigma(z)] \tag{3}$$

coupled with compensating integration

$$T_{minvc}(\ z_i\ ) = \pi\mu \int_0^{z_i} \frac{d}{dz}[z^2\sigma(z)]dz. \tag{4}$$

Both operations are performed numerically. Solution of equation (4) for z_i

provides the "Influential section depth limits estimation" process of the B-connected column of Figure 6 for T_{minvc} being the sample interval and observation duration. The operation is accurate if the quadrature step size is small compared to the lateral extent of the element conductivity. This is accurate since 10 km is small compared to the extents described by the profiles weighed and used from *Lizarralde et al*. [1995]. The one dimensional analysis also accurately resists earth curvature since the depth domain considered is relatively shallow. Since z and $\sigma(z)$ are both always positive, $T_{minvc}(z_i)$ is proportional to z_i. This means a magnetometry sample minimally delayed from one previous to it (for the Nyquist sampling interval) forms a signal diagnostic of the shallowest depth possible. Likewise, magnetic effects of a maximum depth are sensed by a subsequent sample which maximally follows a previous sample. Therefore, for T_{minvc} equaling twice the sampling interval and then the observation survey duration, the incident waves are influenced by upper mantle conductivities between z_{top} and z_{bot} as respective solutions for z_i in equation (4). These depth limits define an influential section of the subsurface which, in a skin depth sense, includes conductivities affecting the incident magnetic signal.

Telford et al. [1982] describe how the horizontal components of magnetic vectors, like the geographic north component of total magnetic intensity B_x, in a half space diminish with depth z by an earth filter multiplier

$$\mathcal{E}_d(j,\omega,\sigma,z) = \exp[-(1+j)\sqrt{\mu\sigma(z)\omega/2}\, z] \qquad (5)$$

with $j = \sqrt{-1}$. Real and imaginary term separation follows as

$$\mathscr{E}_d(j,\omega,\sigma,z) = \exp[-\sqrt{\mu\sigma(z)\omega/2}\,z]\,\{\cos[-\sqrt{\mu\sigma(z)\omega/2}\,z] + j\sin[-\sqrt{\mu\sigma(z)\omega/2}\,z]\}. \quad (6)$$

Like in equation (4), variable conductivity $\sigma(z)$ accommodation is then

$$\mathscr{E}_d(j,\omega,\sigma,z) = \int_{z_{top}}^{z_{bot}} \frac{d}{dz}\{\exp[-\sqrt{\mu\sigma(z)\omega/2}\,z]\cos[-\sqrt{\mu\sigma(z)\omega/2}\,z]\}dz + j\int_{z_{top}}^{z_{bot}} \frac{d}{dz}\{\exp[-\sqrt{\mu\sigma(z)\omega/2}\,z]\sin[-\sqrt{\mu\sigma(z)\omega/2}\,z]\}dz. \quad (7)$$

The quantity $\mathscr{E}_d(j,\omega)$ is called the (lowpass) earth filter over the influential section. This conductive section diffusively (selectively by frequency) converts electromagnetic energy incident to it into that of telluric currents in the section by the Faraday induction law. This is less true for more resistive rock as the telluric energy becomes thermal, but still lost from the surface magnetometer. Accounting for the B loss to the influential section, the equation

$$B_x(j,\omega)\mathscr{E}_d(j,\omega) + B_x(j,\omega)\mathscr{E}_M(j,\omega) = B_x(j,\omega) \quad (8)$$

(with diffusive filter $\mathscr{E}_d$ and diffusion-depleted filter $\mathscr{E}_M$ both acting on the vector component signal) or

$$\mathscr{E}_M(j,\omega) = 1 - \mathscr{E}_d(j,\omega) \quad (9)$$

is used with a (highpass) earth filter at a magnetometry point M $\mathscr{E}_M$. This is the subsurface conductive filter by which incident magnetic signals are changed to those signals observable by magnetometers on the topography. It is the "Influential section magnetic frequency response estimation" process in the B-

connected column of Figure 6. These surface signals are rougher compared to how they would look from a magnetometer at any substantial depth into a subsurface having any conductivity. This is because the electromagnetic earth is a lowpass filter as indicated by the negative sign in equation (5). Using equation (9), the roughening would be anywhere from about 18% to about 29% at a sample interval of 500 s, depending on the local continental geology.

2.3. Incident Magnetic Wave Signal Partial Solution by Least Squares Deconvolution

Since the spatiotemporal domain of the refraction-correlative signals of interest is too small to permit separation of internal and external magnetic fields [*Kaufman and Keller*, 1981], the earth filter should be modeled more stochastically as a linear system in time t

$$\Delta B_{xiM}(t) * \mathscr{E}_M(t) = \Delta B_{xdwM}(t). \tag{10}$$

Equation (10) convolves the magnetic anomaly signal at point M, ΔB_{xiM}, with earth filter $\mathscr{E}_M$ to obtain the de-whorled anomaly component at M, ΔB_{xdwM}. Equation (10) also describes the attenuation of temporal geomagnetic variations such as bays and pulsations by the conducting subsurface. The quiet daily variation content of the heliosynchronous ionospheric plasma whorls [*Telford et al.*, 1982] produces the magnetic field component to which ΔB_{xdwM} is anomalous. *Tarits' and Grammatica's* [2000] model, spherical harmonic to degree and

(positive and negative) order 4, globally quantifies the magnetic fields of the whorls. These are most active during daylight during which the field magnetometry was performed. Least squares deconvolution for the ΔB_{xiM} solution in t is not discriminating (allows no interpretive intervention) and is very memory-intensive. In the ω domain, the equation (10) convolution changes to multiplication as

$$\Delta B_{xiM}(j,\omega)\mathscr{E}_M(j,\omega) = \Delta B_{xdwM}(j,\omega) \tag{11}$$

This equates the second term in equation (8) to conventionally-processed data and forms the linear system.

After some common substitutions and algebra,

$$|\mathscr{E}_M(j,\omega)|\exp\{j\varphi[\mathscr{E}_M(j,\omega)]\}|\Delta B_{xiM}(j,\omega)|\exp\{j\varphi[\Delta B_{xiM}(j,\omega)]\} = |\Delta B_{xiM}(j,\omega)| \times \exp\{j \times \varphi[\Delta B_{xdwM}(j,\omega)]\} \tag{12}$$

follows to separate the magnitudes (in absolute value bars) from the phase angles φ, all functions of complex arguments. Combining exponentials, taking natural logarithms, and equating real and imaginary terms yield the simultaneous pair of equations

$$\ln|\Delta B_{xiM}(j,\omega)| = \ln|\Delta B_{xdwM}(j,\omega)| - \ln|\mathscr{E}_M(j,\omega)|, \tag{13a}$$
$$\varphi[\Delta B_{xiM}(j,\omega)] = \varphi[\Delta B_{xdwM}(j,\omega)] - \varphi[\mathscr{E}_M(j,\omega)]. \tag{13b}$$

Random $\varphi[\Delta B_{xdwM}(j,\omega)] = 0$ in a least squares sense across the entire ω domain because zero is mean to the $\tan^{-1}$ function range. This makes equations (13) actually

$$|\Delta B_{xiM}(j,\omega)| = |\Delta B_{xdwM}(j,\omega)|/|\mathscr{E}_M(j,\omega)|, \quad (14a)$$
$$\varphi[\Delta B_{xiM}(j,\omega)] = -\varphi[\mathscr{E}_M(j,\omega)] \quad (14b)$$

after taking the exponent of both sides of the first equation. This is the "Division and negation" process of the C-connected column of Figure 6. The "Band of interest selection" process assures that the most predictable (lowest frequency) and most correlation-possible sinusoids are chosen. The selected amplitude spectrum, modeled as an infinitely-dense comb function, and the empirically logarithmic [*Von Seggern,* 1993] phase spectral function respectively produce

$$\sum_{n=1}^{\infty} c_n \delta|\omega - \omega_n| = |\Delta B_{xdwM}(j,\omega)|/|\mathscr{E}_M(j,\omega)|, \quad (15a)$$
$$(\omega/|\omega|)\log_{k_1}(k_2\omega) = \varphi[\Delta B_{xiM}(j,\omega)] \quad (15b)$$

with arbitrarily positive constants c_n and yet unknown real constants k_1 and k_2. This is the "Spectral type differentiation" process of the C-connected column of Figure 6. Properties of logarithms yield, after some algebra,

$$\sum_{n=1}^{\infty} c_n \delta|\omega - \omega_n| = |\Delta B_{xdwM}(j,\omega)|/|\mathscr{E}_M(j,\omega)|, \quad (16a)$$
$$\varphi[\Delta B_{xiM}(j,\omega)](|\omega|/\omega)\ln k_1 - \ln k_2 = \ln\omega. \quad (16b)$$

Solutions k_1 and k_2 arise after m (≥ 2) discrete selections of ω over the zero to positive Nyquist angular frequency ω_N domain and their corresponding φ data are substituted in simultaneous equations (16b). This system factors into the matrix equation

$$PL = W \tag{17}$$

with

$$P = \begin{bmatrix} \varphi[\Delta B_{xiM}(j,\omega_1)] & -1 \\ . & . \\ . & . \\ . & . \\ \varphi[\Delta B_{xiM}(j,\omega_m)] & -1 \end{bmatrix}, \quad L = \begin{bmatrix} \ln k_1 \\ \ln k_2 \end{bmatrix}, \quad \text{and} \quad W = \begin{bmatrix} \ln \omega_1 \\ . \\ . \\ . \\ \ln \omega_m \end{bmatrix}.$$

The least squares solution ("(Logarithmic) least squares modeling" of the C-connected column of Figure 6) is

$$L = (P^{\mathrm{T}}P)^{-1}P^{\mathrm{T}}W \tag{18}$$

before

$$\begin{aligned} k_1 &= \exp(L_1) \\ k_2 &= \exp(L_2). \end{aligned} \tag{19}$$

Evaluation of fit functions subscripted *f*

$$\begin{aligned} [\Delta B_{xiMf}(j,\omega)] &= \sum_{n=1}^{\infty} c_n \delta|\omega - \omega_n|, \\ \varphi[\Delta B_{xiMf}(j,\omega)] &= (\omega/|\omega|)(\ln k_2 + \ln\omega)/\ln k_1 \end{aligned} \tag{20}$$

completes the deconvolution in ω. While done separately, Gaussian fitting of both amplitude and phase is effectively achieved since individual comb singularities in the frequency domain approximate very damped statistical bell curves. Upon inverse Fourier transformation (right before the C connector in

Figure 6), equation (16a) becomes

$$\Delta B_{xiM}(t) = \sum_{n=1}^{\infty} c_n \cos[\omega_n t + (\omega_n/|\omega_n|)(\ln k_2 + \ln\omega_n)/\ln k_1] \quad (21)$$

or

$$\Delta B_{xiM}(t) = \sum_{n=1}^{\infty} c_n \cos\{(\omega_n t) + \varphi[\Delta B_{xiMf}(j,\omega_n)]\}. \quad (22)$$

Because c_n is arbitrary and there are multiple normalizations for an inverse Fourier transform, no quantities or error bars can be assigned to the isolated magnetic anomaly $\Delta B_{xiM}(t)$ ordinates. Only the relative magnitudes of the magnetic intensities along the signal are important. $\Delta B_{xiM}(t)$ is like a seismic signal in that respect.

2.4. Incident Magnetic Wave Signal Completed Solution by Angular Frequency Selection

In the frequency band of interest (Figure 5), frequency generally controls the type of ionospheric electron movement. The lower frequency whorls, bays and pulsations result from horizontal and fluid-like vortices that are, to some spatiotemporal resolution, predictable by *Tarits and Grammatica* [2000]. Higher frequency and smaller individual pulsations occur from electron gyration along main earth magnetic field flux lines (Figure 3). This is known as Alfven pulsation electron movement [*McPherron*, 2002] and correlates better with GPS refraction. It is also shown on Figure 8.

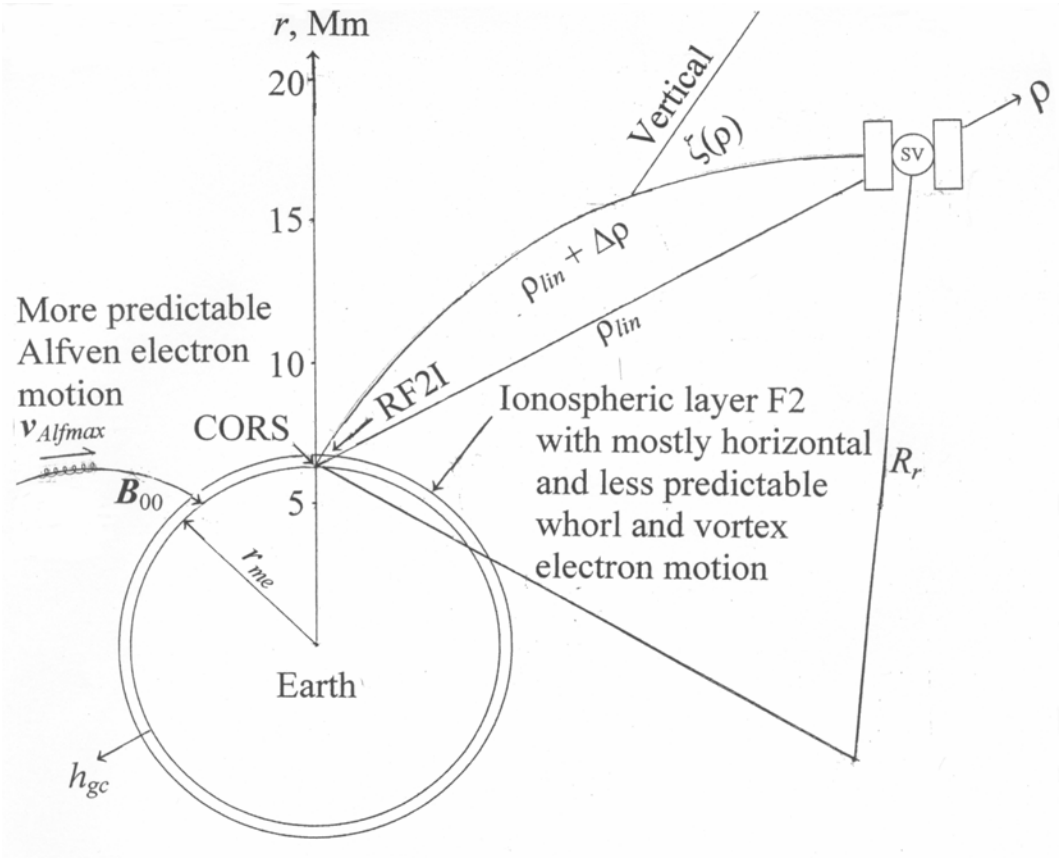

Figure 8. Simplified aeronomic geometry with ionospheric height and GPS range refraction exaggerated [*Kivelson and Southwood*, 1991; *Bassiri and Hajj*, 1993; *McPherron*, 2002]. Continuously operating reference station is abbreviated CORS. Range- (ionospheric layer) F2 intersection is abbreviated RF2I. The maximum Alfven pulse velocity is v_{Alfmax} and $\boldsymbol{B}_{00}$ is the main earth magnetic field. The single difference unrefracted range is ρ_{lin} with anomaly of refraction $\Delta\rho$. R_r is the radius of the exaggerated and simplified refraction. The earth mean radius is r_{me} and h_{gc}, the height in excess of it. The zenith angle of the CORS-to-SV refracted range is ς . The CORS-to-SV elevation angle is η. The CORS-to-SV earth centered vertex angle is ψ. The SV is r_{SV} from the earth center. The Cartesian coordinate system is earth centered and includes the CORS and SV in its first quadrant.

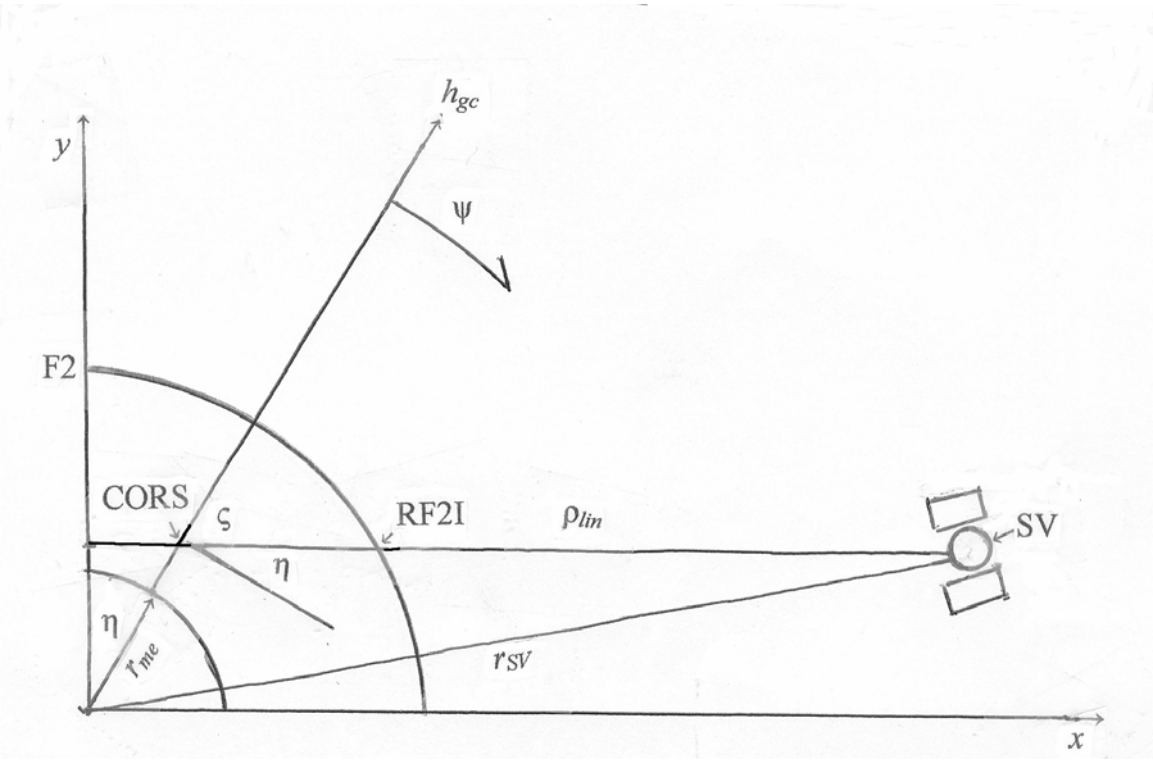

Figure 8. Continued.

The Alfven system of the wave fitting is based on domains of zero or near zero curvature of a selected complex spectral component. The migration of the electron gyrations along the flux lines should produce, in the band of our interest, predominantly linear functions of time. The Fourier transforms $\mathfrak{I}$ of these are also predominantly linear. (See any pictorial dictionary of Fourier transforms.) This is because, as sums of sinusoids, any curved variations in time provide the gradual (and also curved) amplitude maximums of the sinusoids for their real and imaginary spectra. With successive use of the Fourier algorithm

over the zero to ω_N interval, there is therefore nothing to alter the curvature (or lack thereof) of the transformed function of t. Examples [*Bracewell,* 1986] of these pairs in this interval are predominantly linear

$$\Im[\sin^2(\omega_N t)/(\omega_N t)^2] \;=\; 1 - \omega\,/\omega_N \tag{23}$$

(Figure 9) and predominantly curved

$$\Im(t^{-1/2}) \;=\; -j\omega^{-1/2} \tag{24}$$

(Figure 10).

Most data signals, however, Fourier transform into both real and imaginary component functions. From equation (21), the curvature of these are

$$\frac{\partial^2}{\partial\omega^2}\mathrm{Re}[\Delta B_{xiM}(j,\omega)] \;=\; \frac{\partial^2}{\partial\omega^2}\mathrm{Re}\{\,\Im\sum_{n=1}^{\infty}\; c_n\cos[\omega_n t + (\omega_n/|\omega_n|)(\ln k_2 + \ln\omega_n)/\ \ln k_1]\} \tag{25}$$

or

$$\frac{\partial^2}{\partial\omega^2}\mathrm{Im}[\Delta B_{xiM}(j,\omega)] \;=\; \frac{\partial^2}{\partial\omega^2}\mathrm{Im}\{\,\Im\sum_{n=1}^{\infty}\; c_n\cos[\omega_n t + (\omega_n/|\omega_n|)(\ln k_2 + \ln\omega_n)/\ \ln k_1]\}. \tag{26}$$

These equations express the "Real/imaginary" data and the "Curvature" process in the C-connected branch of Figure 6.

The extreme but unavoidable scarcity of the GPS control (only several SVs close to the magnetic survey point M) in the solid angle of the celestial hemisphere requires truncation of these equations upper limit to $n = 1$ for satisfactory correlation with GPS refraction data. This is because the entire magnetometer-sensitive ionosphere must be abbreviated by only several (n_{SV})

GPS range-ionosphere intersections; the abbreviation is virtually 1:∞. This is the "Abbreviation" manual process on the C-connected column of Figure 6.

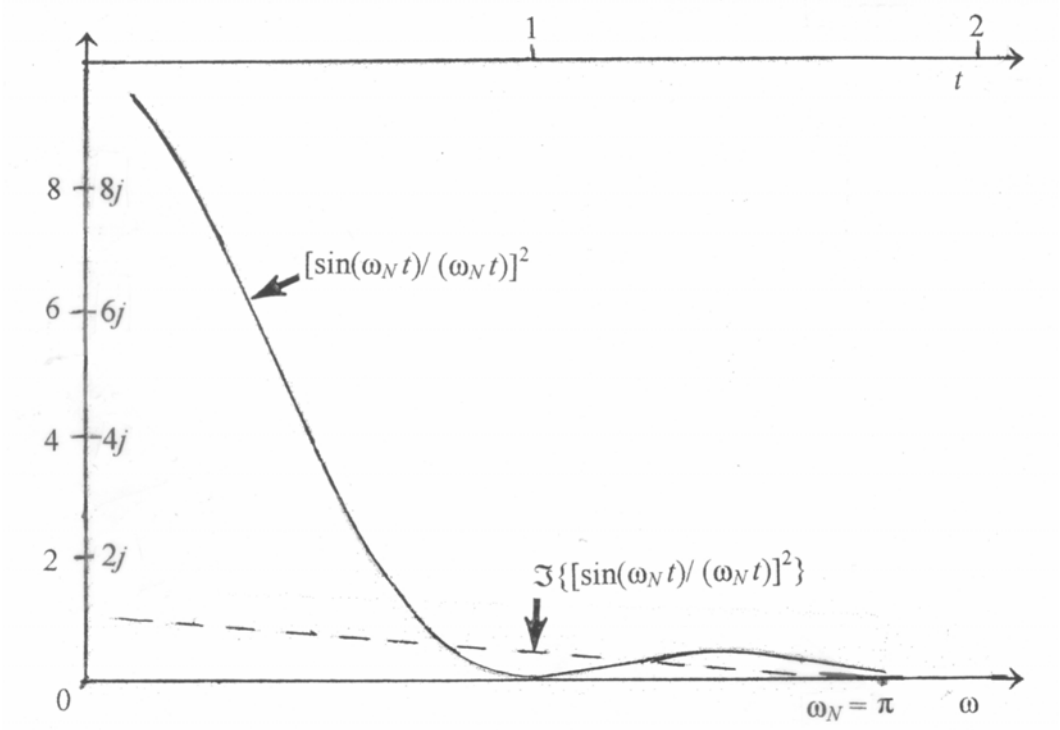

Figure 9. Fourier transform pairs predominantly linear over lower angular frequencies ω; the signal is solid and the spectrum is dashed.

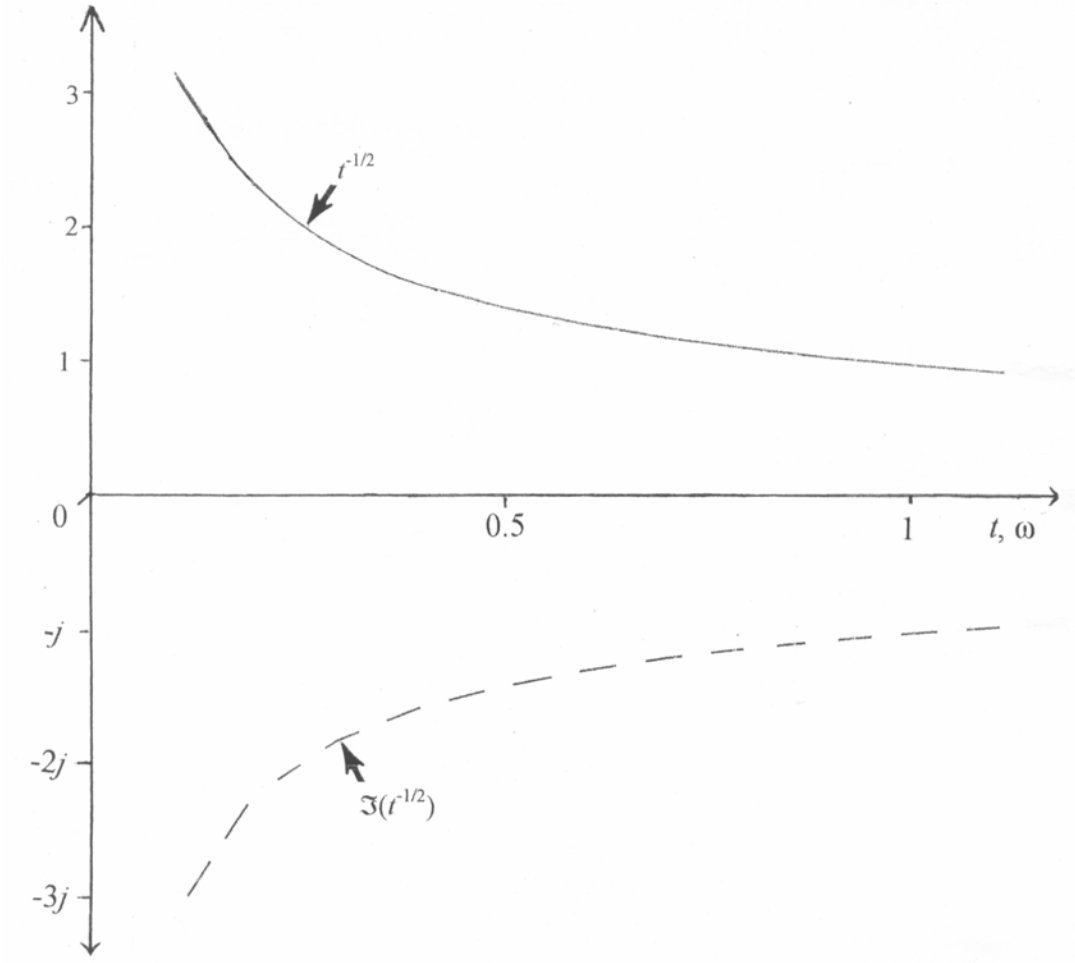

Figure 10. Fourier transform pairs predominantly curved over lower angular frequencies ω; the signal is solid and the spectrum is dashed.

The (single therefore) constant c_1 has become unity for simplicity since signals ultimately derived from non-phase and non-filter spectra can have any gain applied to them for correlation purposes only. The lower angular frequency limit of non-curvature ω_1 is interpreted to be the best-recognizable lower limit of a domain of zero

or near-zero curvature considering both equations (25) and (26) plots in the Results section. At this limit, the relationship between Figures 9 and 10 strongly suggests the more linear Alfven electron motion.

2.5. Global Positioning System (GPS)

The online availability of GPS space vehicle (SV) ephemerides (position records) and range (observed SV to GPS receiver) online pseudorange data [*National Geodetic Survey (NGS),* 2003, 2004] affords study of artificial electromagnetic wave refraction in the ionosphere. Artificial waves are more diagnostic of ionospheric refraction than natural waves since the position of the wave source is known. The GPS receivers are located at NGS continuously operating reference stations (CORS). The refraction of electromagnetic waves is also dependent on the main earth diurnally-relatively magnetostatic vector (International Geomagnetic Reference Field 2000 (IGRF) 2000)) [*Bassiri and Hajj*, 1993] that is also available online from the *National Geophysical Data Center* (*NGDC*) [2003, 2004].

Figure 6 shows how these GPS range and main earth magnetic data can be input to both conventional and SCIRCMS processing techniques that can reveal two important descriptions for the refractions corresponding to each magnetometry sample time. These descriptions are the position and the amount of the GPS range refraction.

Maximum GPS range refraction occurs in the densest layer of the ionosphere: its F2 layer, about 300 to 350 km above the solid earth. The first important refraction description is the solution for the range-F2 [*Bassiri and Hajj*, 1993] intersection (RF2I).

The law of sines applies to Figure 8 as

$$r_{SV} / \sin(180° - \varsigma) = \rho_{SV} / \sin(\psi_{SV}). \quad (27)$$

After some trigonometry, the CORS-to-SV elevation angle is

$$\eta = 90° - \sin^{-1}[r_{SV} \sin(\psi_{SV}) / \rho_{SV}]. \quad (28)$$

Along the *y* axis,

$$y_{CORS} = (r_{me}) \cos(\eta) \quad (29)$$

results. By the Pythagorean theorem, with layer F2 being r_{F2} from the earth center,

$$x_{CORS} = (r_{F2}^2 - y_{CORS}^2)^{1/2} \quad (30)$$

can be substituted to get the CORS-to-F2 range

$$\rho_{F2} = x_{CORS} - (r_{me} + h_{gcCORS}) \sin(\eta). \quad (31)$$

Since the earth centered, earth fixed (ECEF) coordinates are known for both CORS and SV: X_{CORS}, Y_{CORS}, Z_{CORS}, X_{SV}, Y_{SV}, Z_{SV},

$$X_{RF2I} = X_{CORS} + \rho_{F2} \cos(\alpha_{CORSSV}) \quad (32a)$$
$$Y_{RF2I} = Y_{CORS} + \rho_{F2} \cos(\beta_{CORSSV}) \quad (32b)$$
$$Z_{RF2I} = Z_{CORS} + \rho_{F2} \cos(\gamma_{CORSSV}), \quad (32c)$$

with CORS-to-SV direction angles α_{CORSSV}, β_{CORSSV}, and γ_{CORSSV}. This is the "RF2I coordinates solution" process in Figure 6. The selection of SVs and

CORSs was done to maximize the azimuthal variation of RF2I segments (RF2IS) (sequences of RF2I points between the CORS and one SV) around each survey point M. Since the magnetometry Nyquist frequency exceeds that temporal quantity of the ephemerides, the latter records require interpolation. *Seeber* [1993] quadratic polynomial fitting provides denser ephemerides over time. The multiplicity of RF2ISs, together with the resampling of SV positions, greatly lessens random error in subsequent processing.

The second important refraction description is the de-whorled GPS range, the anomaly of which includes mostly refraction from the F2. The GPS is used in its autonomous (neither differential nor phase) mode. The standard SV and receiver clocks correction [*NGS*, 2003], of pseudoranges to ranges ρ by adding the clock error range to the P code, L2 frequency pseudorange. This is the "Clocks correction" process in Figure 6; the magnitude of the correction to the SV clock is on the order of tens of microseconds. The CORS clock error drifts to about 1 millisecond in 30 minutes. The "(Quadratic) position resampling to magnetometry times" follows as quadratic polynomials [*Seeber*, 1993] are fit between three ephemerides points to resample the SV positions from the ephemerides to the positions to magnetometry sample times. Removal of the CORS-to-SV distance ρ_{lin} (the "SV-receiver distance subtraction" process) from the interpolated ranges provides a range anomaly $\Delta\rho = \rho - \rho_{lin}$. An approximation of the earth's gravitation to a spherical harmonic expansion to

degree and order 6 [*Seeber*, 1993] between ephemerides points is made to have a linear range effect for the ”(Linear) spherical harmonic effect modeling and removal” process. Since the CORS is not geocentric and the SV orbit is more so, a hyperbolic range anomaly component is eliminated in the “Hyperbolic effect removal” by the law of cosines. The same magnetic diurnal and whorl effects affect the range anomaly as the magnetic anomaly. This is why a cubic polynomial achieves the (linear) diurnal effect modeling and removal and the (quadratic) whorl effect modeling and removal” processes for GPS range anomalies to be most diagnostic over close-to-M RF2I durations. These two steps are combined in the “(Cubic) diurnal and whorl effects modeling and removal” process.

Pseudomagnetic anomaly signal synthesis is shown in the continuation of Figure 6. An SV, CORS, RF2I, and M comprise the most critical elements of the SCIRMCS geometry (Figure 11).

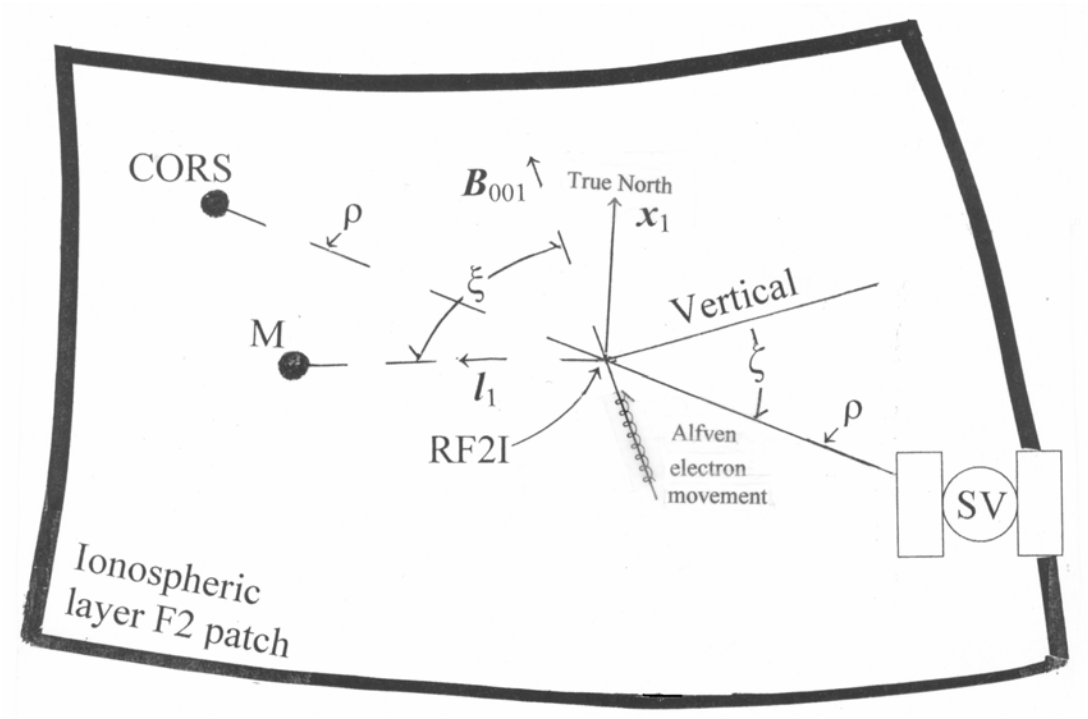

Figure 11. CORS-SV-M aeronomic geometry relating to the earth's ionospheric layer F2. RF2I is not only contained in range ρ but is the vertex for angle ξ between the IGRF 2000 earth magnetic intensity unit vector $\boldsymbol{B}_{001}$ and RF2I-to-M unit vector $\boldsymbol{l}_1$. Range ρ continues to the SV at zenith angles ζ.

The "Pseudomagnetic anomaly signal synthesis" process (immediately before the D connector) uses the Biot-Savart law (*Lorrain and Corson*, 1970):

$$\boldsymbol{B}_a = [\mu_0/(4\pi)]\, I_a \oint_a (\boldsymbol{dl}_a \times \boldsymbol{r}_1) / r^2 \qquad (33)$$

as its basis. $\boldsymbol{B}_a$ is the magnetic intensity due to a circuit *a*; the magnetic permeability of free space is μ_0. I_a is the current in circuit *a*, $\boldsymbol{dl}_a$ is a length element of the circuit in the direction of the current and *r* is the length between

$\boldsymbol{dl}_a$ and the evaluation point with $\boldsymbol{r}_1$ the $\boldsymbol{dl}_a$-to-observation point unit vector. *Lorrain and Corson* adapt the law to a non-circuital flow of free electrons, making the ionospheric magnetic intensity effect at the magnetometry point M

$$\boldsymbol{B}_M = \mu_0 \int_V (\mathbf{J}_f \times \boldsymbol{l}_1)/l^2 \, dV/(4\pi) \tag{34}$$

(with free electron current density vector $\mathbf{J}_f$, and circum-RF2I volume V) is illustrated in Figure 11. $\mathbf{J}_f$ is the product of F2 refraction-dependent free electron density and the velocity of the free electron assemblage. The adaptation expresses the magnetic field due to even distantly passing ions.

A coefficient of refraction derived from *Torge* [1991]

$$c_r = r_{me}\{24[(\rho_{lin} + \Delta\rho)^{-2} - \rho_{lin}/(\rho_{lin} + \Delta\rho)^3]\}^{1/2} \tag{35}$$

(Figure 8) is also the ratio r_{me}/R_r [*Bomford*, 1985]. (The mean earth radius is r_{me}, the radius of refraction is R_r, the unrefracted range is ρ_{lin} and $\Delta\rho$ the anomaly of refraction..) *Bomford* also establishes a proportionality between the coefficient of refraction c_r and the geocentric height derivative of electron density $dN_e(h_{gc})/dh_{gc}$. At the analysis height above the mean earth sphere h_{gc} = 300 km (below most any estimate of the $N_e(h_{gc})$ maximum), a property of simplified ionospheric models [*Ramo et al.,*1984; *Hajj and Romans*, 1996] is $N_e(h_{gc}) \; \alpha \; dN_e(h_{gc})/dh_{gc}$. Transitively then, $c_r \; \alpha \; N_e$, making

$$c_r \; \alpha \; \Delta N_e. \tag{36}$$

Since each RF2I is ideally a surface-line segment (range) intersection point,

the equation (34) volume derivative

$$d\boldsymbol{B}_M = \mu_0 (\mathbf{J}_f \times \boldsymbol{l}_1)/(4\pi l^2) \tag{37}$$

applies to the unit volume around each RF2I. Expanding the current density yields, with the charge, density, and maximum Alfven (predictable electron) (Figure 8) speed q_e, ΔN_e, and v_{Alfmax} respectively, of the free electrons,

$$\Delta\boldsymbol{B}_M = \mu_0 (q_e \Delta N_e v_{Alfmax} \boldsymbol{B}_{001} \times \boldsymbol{l}_1)/(4\pi l^2). \tag{38}$$

Expanding the north component of this cross product with $v_{Alfmax} = [B_{00}^2/(\mu_0 N_e)]^{1/2}$ [McPherron, 2002] in general factors and arguments of aeronomic GPS (Figures 8 and 11) quantities is, over time t, the partial pseudomagnetic anomaly signal

$$\Delta B_{pxM}(t) = \mu_0 q_e c_r[\rho_{lin}(t),\Delta\rho(t)] v_{Alfmax}\{B_{00},c_r[\rho_{lin}(t),\Delta\rho(t)]\}\sin(I_{00})\sin\xi(t)/[4\pi l^2(t)]. \tag{39}$$

B_{00} is the diurnal-relatively magnetostatic IGRF 2000 magnetic total intensity (with $\boldsymbol{B}_{001}$ its unit vector); similarly, the inclination is I_{00}. Summing for each of the several k-indexed RF2IS,

$$\Delta B_{pxM}(t) = \sum_{k=1}^{n_{SV}} \Delta B_{pxMk}(t) \tag{40}$$

abbreviates equation (34) integration. This is the total pseudomagnetic anomaly signal. Because of the proportionalities which produce its c_r argument, no quantities or error bars can be assigned to total or partial pseudomagnetic anomaly ordinates. Only the relative magnitudes of the ordinates along the signal are important. $\Delta B_{pxM}(t)$ is like a seismic signal in that respect. The

summation also reduces noise from the random but unavoidable residual errors of the SV clocks and range multipaths. The most significant relationship is

$$\Delta B_{pxM}(t) \ \alpha \ \Delta B_{xiM}(t) \tag{41}$$

after isolation (restoration of the low frequency magnetic component to the subsurface).

2.6. Correlative Evaluation

The flow union near the end of Figure 6 describes a single statistical evaluation of the magnetic isolation with respect to more of an independent method of monitoring atmospheric electron movement: that of monitoring GPS ranges. This is a better (external) way to evaluate $\Delta B_{xiM}(t)$ than internally propagating error bars through the development of this signal, even if such a propagation were possible.

The $\Delta B_{xiM}(t)$ ordinates are first equalized (having their mathematical function range proportioned) to those of $\Delta B_{pxM}(t)$. Cross correlation [*Robinson*, 1983] of the two data anomaly signals becomes the numerator of a fraction, the denominator of which is the autocorrelation of $\Delta B_{pxM}(t)$. If necessary, the reciprocal of the quotient provides a percent fit less than 100.

3. RESULTS

Texas affords a diversity of geology and petrology to test SCIRCMS over both relatively conductive sedimentary rock and relatively resistant igneous rock. While the influential sections of both are mostly in the upper mantle, *Lizarralde et al.* [1995] depict substantially different conductivities for them. Because of multiple Fourier and inverse Fourier transform amplitude normalizing techniques, only the observed and de-whorled magnetic, conductivity, earth filter and phase plots will have their independent axes enumerated.

3.1 Initial Results

3.1.1 Sedimentary Basin: Butler Bayou

Located near the Gulf Coastal Plain (Figure 9a) the Butler Bayou station BB occupies a point M (Figure 12) upon Quaternary fluvial deposits [*Renfro*, 1973] which overlie a variety of consolidated sediments about 15 km thick [*Worrall and Snelson*, 1989]. This overlays at least 15 more km of continental crust (Figure 12).

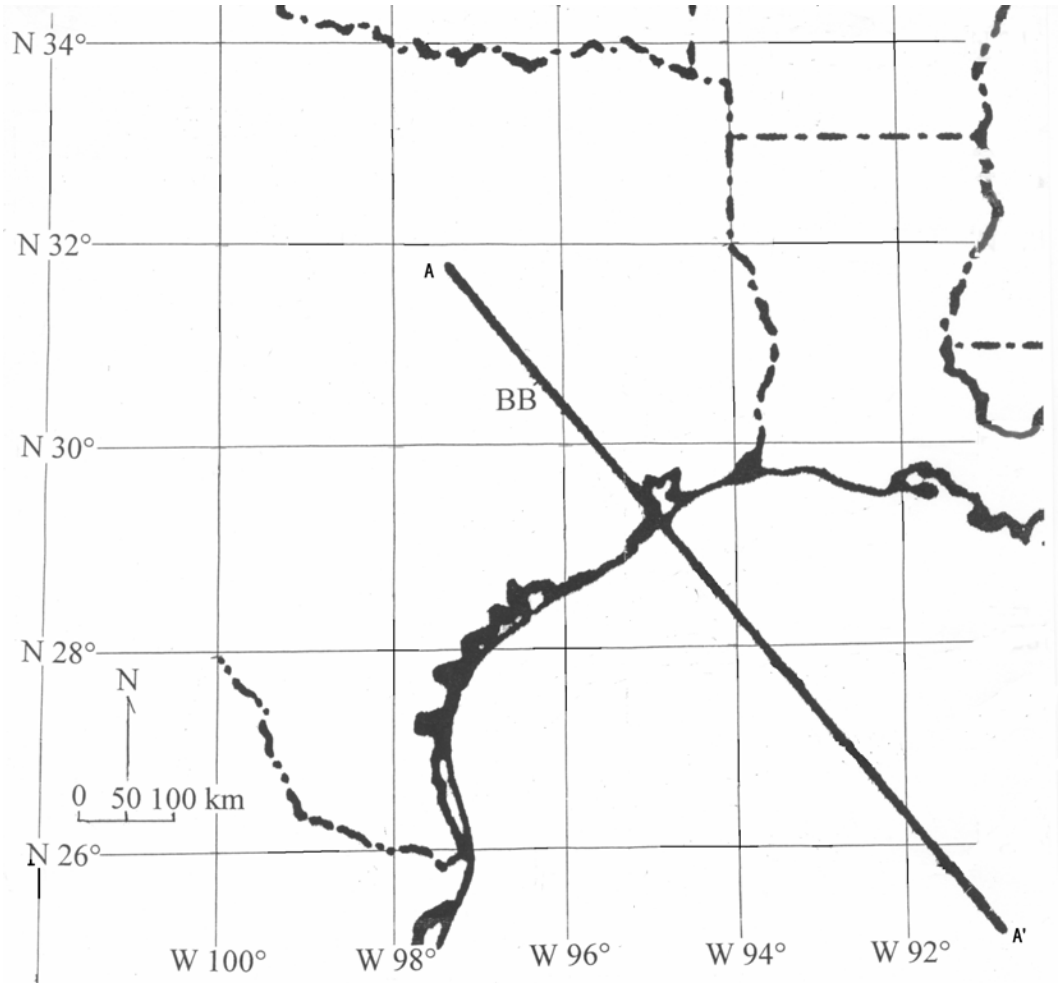

Figure 12. Geographic and geologic setting of the Butler Bayou (BB) study station. (Reprinted with permission from *The Geology of North America; An Overview, D. M. Worrall and S. Snelson,* 1989, Geological Society of America, Boulder, CO, 1989, Geological Society of America.) United States Geological Survey (USGS) "Chances Store" 7.5 minute topographic quadrangle, 1980 (no copyright).

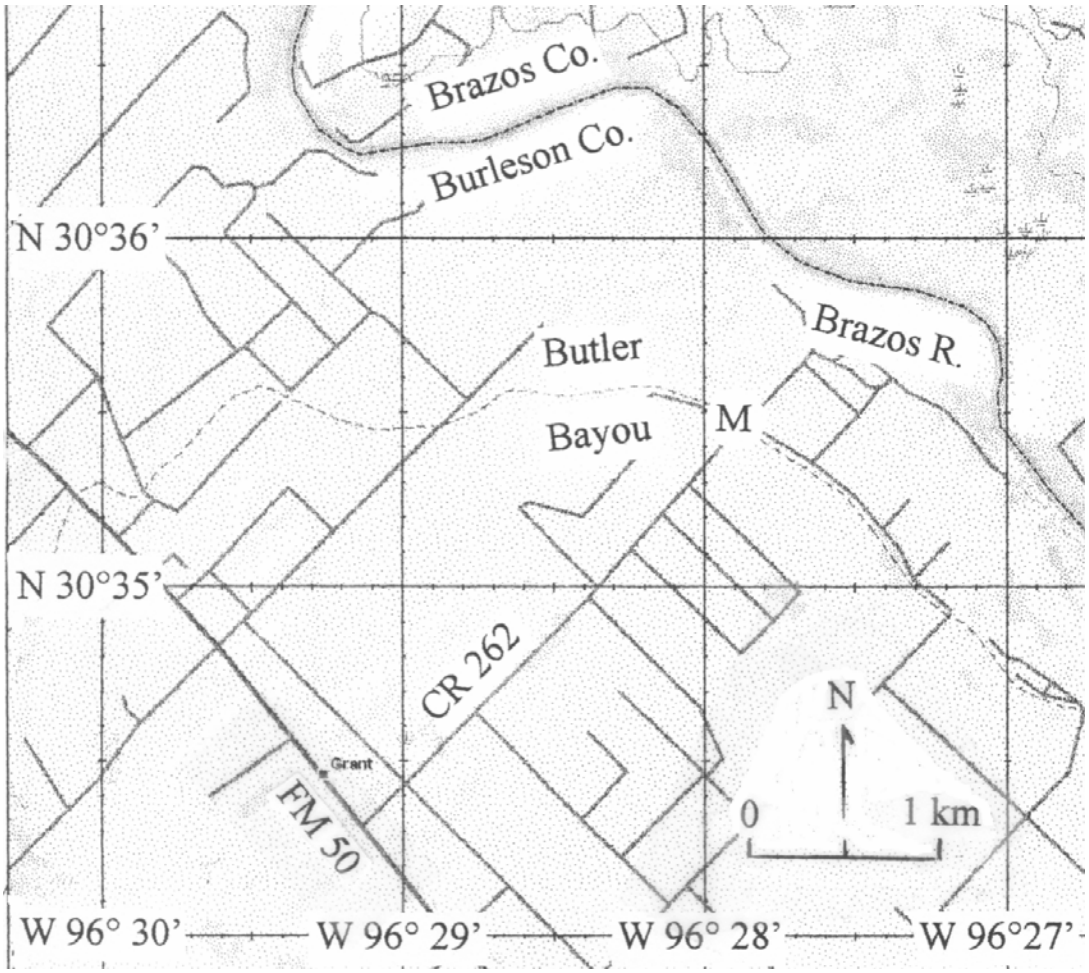

Figure 12. Continued.

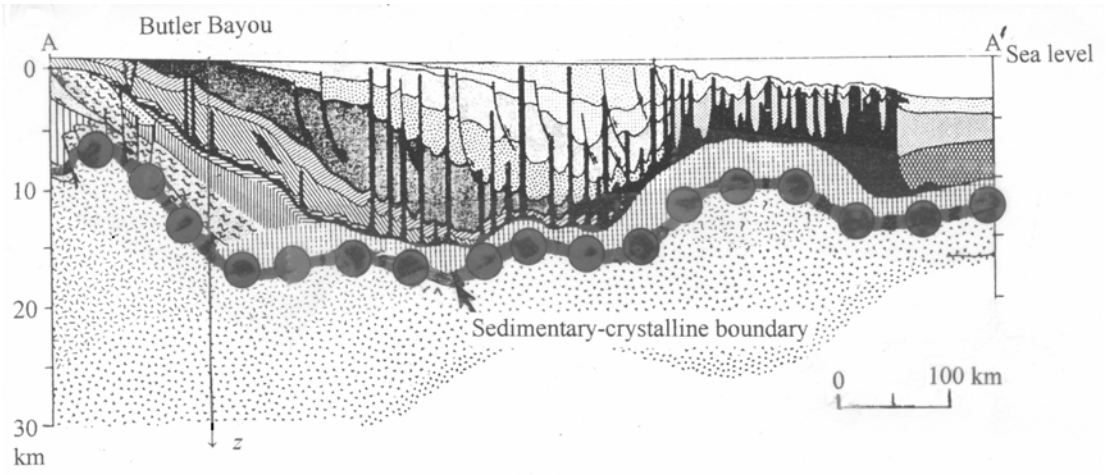

Figure 12. Continued.

Figure 13 shows the conductivities of the basin with two resistive singularities: those of the Louann salt and the Moho.

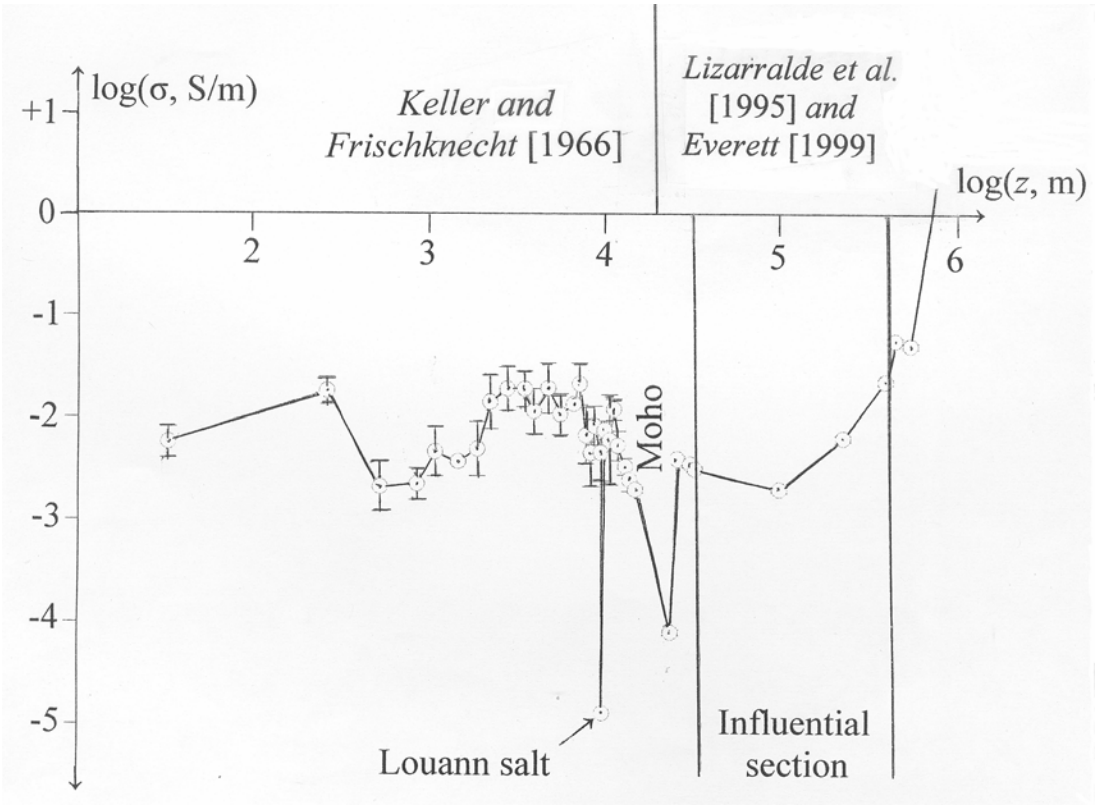

Figure 13. Butler Bayou conductivity profile with 95% confidence error bars where available along its Figure 12 depth axis. The shallow data source is a laboratory and the deeper data source is a weighting of two magnetotelluric inversions from Carty Lake, Ontario (40%) and Tucson, Arizona (60%).

The magnetic data display from Butler Bayou begin with that of the observed anomaly signal of Figure 14, the sample interval of which is 5 s.

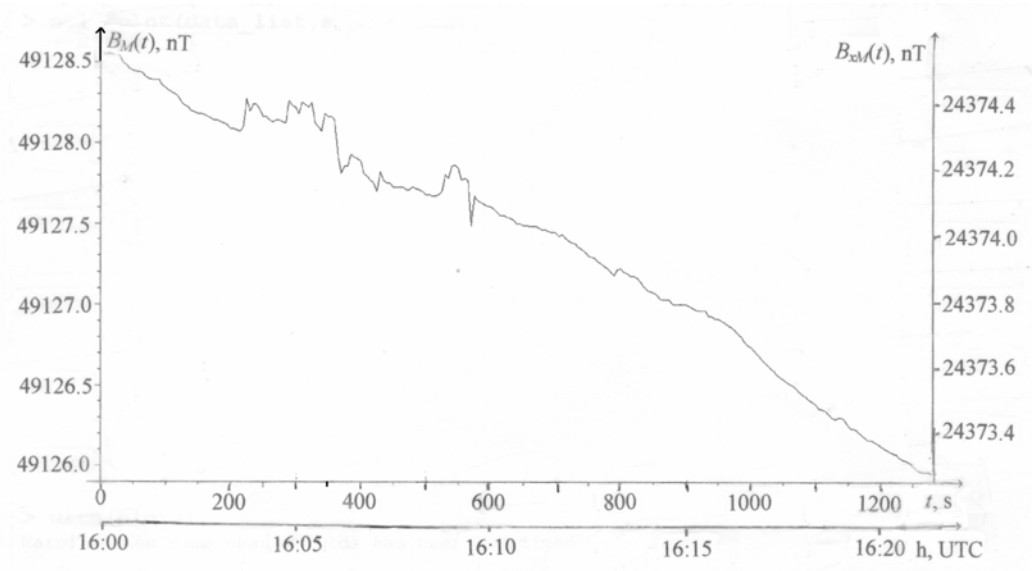

Figure 14. Observed magnetic anomaly data signal at Butler Bayou M. The 90% confidence error is approximately ±0.01 nT.

Of particular note is the removal of the strong trend in Figure 15 for the

(stationary) de-whorled magnetic anomaly signal.

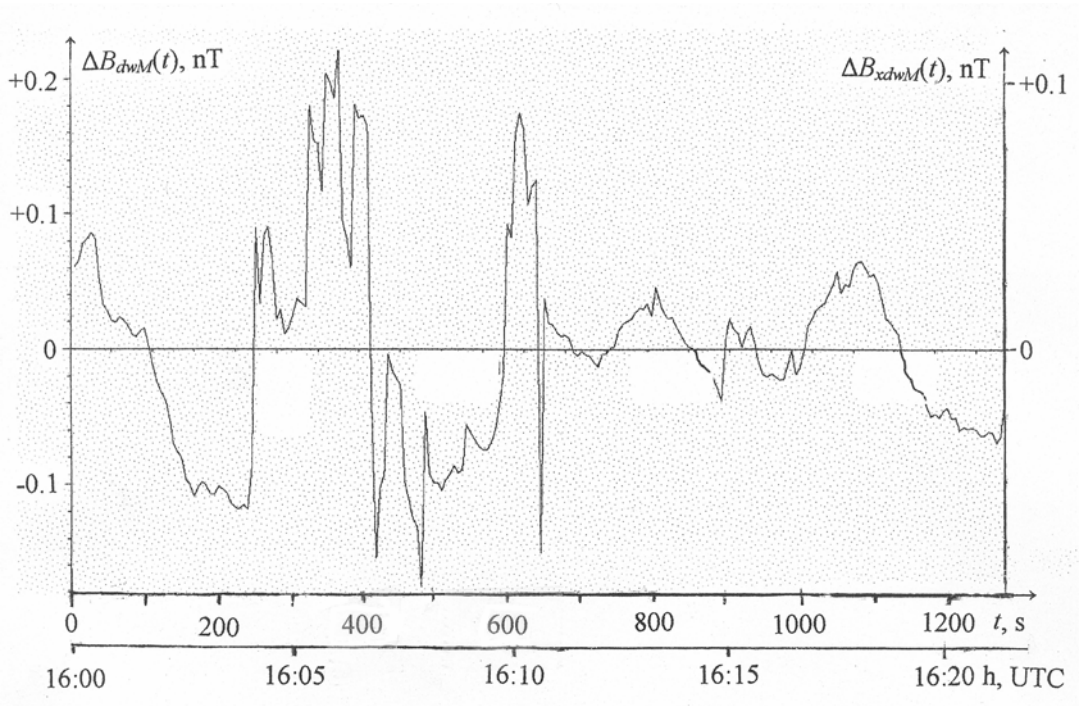

Figure 15. De-whorled magnetic anomaly signal and its north component at Butler Bayou M. The 90% confidence error is approximately ±0.01 nT.

Figure 16 shows the amplitude spectrum and an empirical continuum from zero to the Nyquist frequency. The phase spectrum is randomly trivial (composed of many noise-resembling $\tan^{-1}$ functions) and therefore omitted.

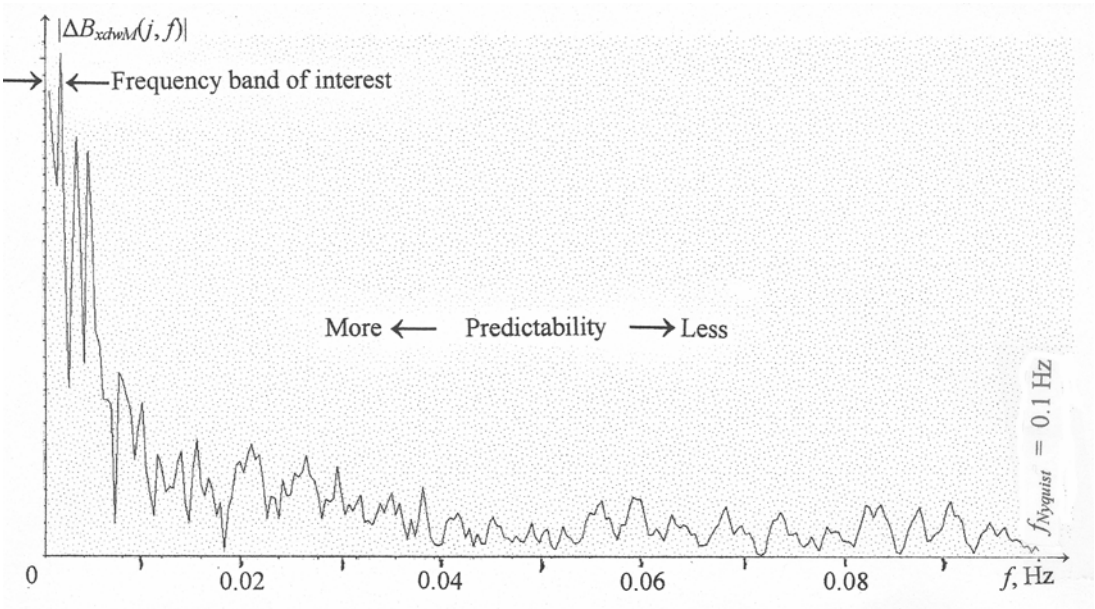

Figure 16. Amplitude spectrum (to the Nyquist frequency) of the de-whorled magnetic anomaly signal at Butler Bayou M.

Focusing on the frequency band of maximum predictability, Figure 17 includes the phase spectrum.

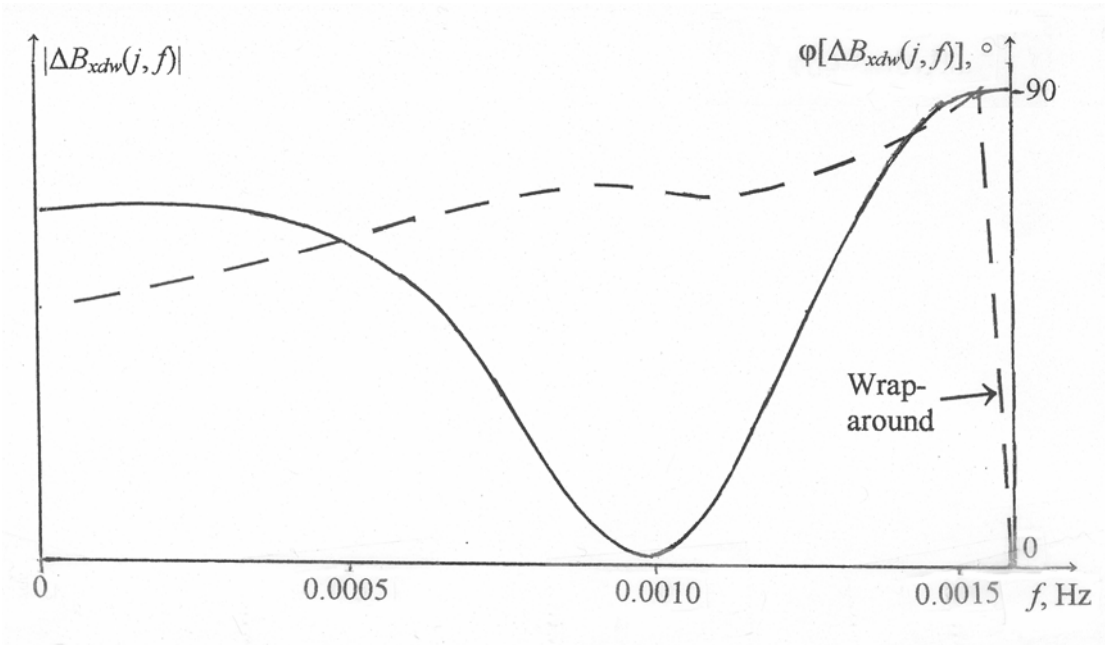

Figure 17. Amplitude (solid) and phase (dashed) spectral band of interest of the de-whorled magnetic anomaly data signal at Butler Bayou M. The data are smooth due to the lack of a variety of sinusoids in this band.

The application of equations (4) and (7) on the data of Figure 15 produce the amplitude and phase spectra of Figure 18: the earth filter at depth (right below the influential section).

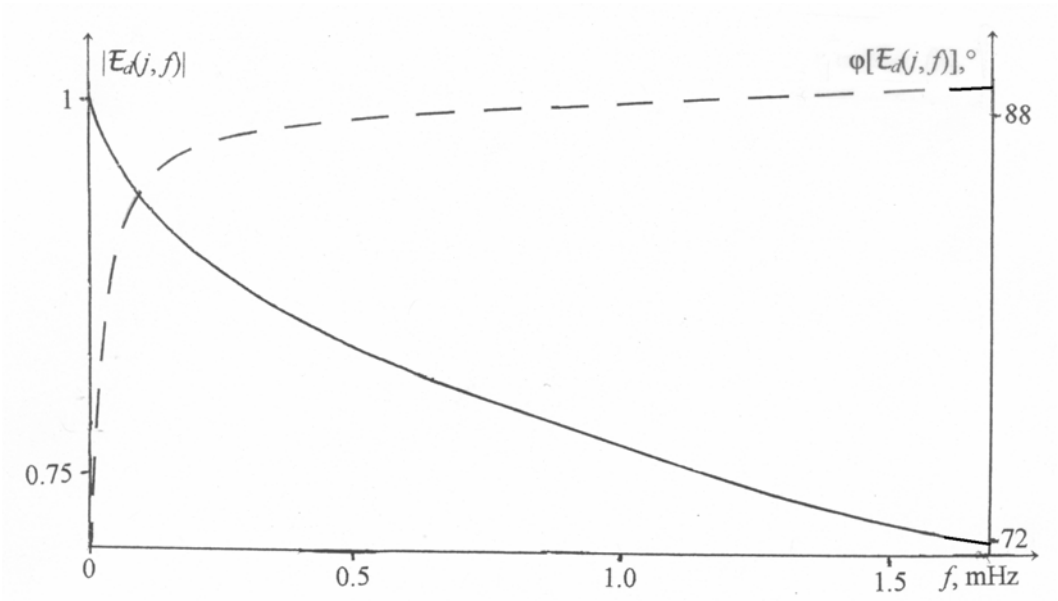

Figure 18. Amplitude (solid) and phase (dashed) spectral band of interest of the earth filter at the base of the influential section beneath Butler Bayou M**.**

Equation (9) then provides the earth filter at the magnetometer: Figure 19.

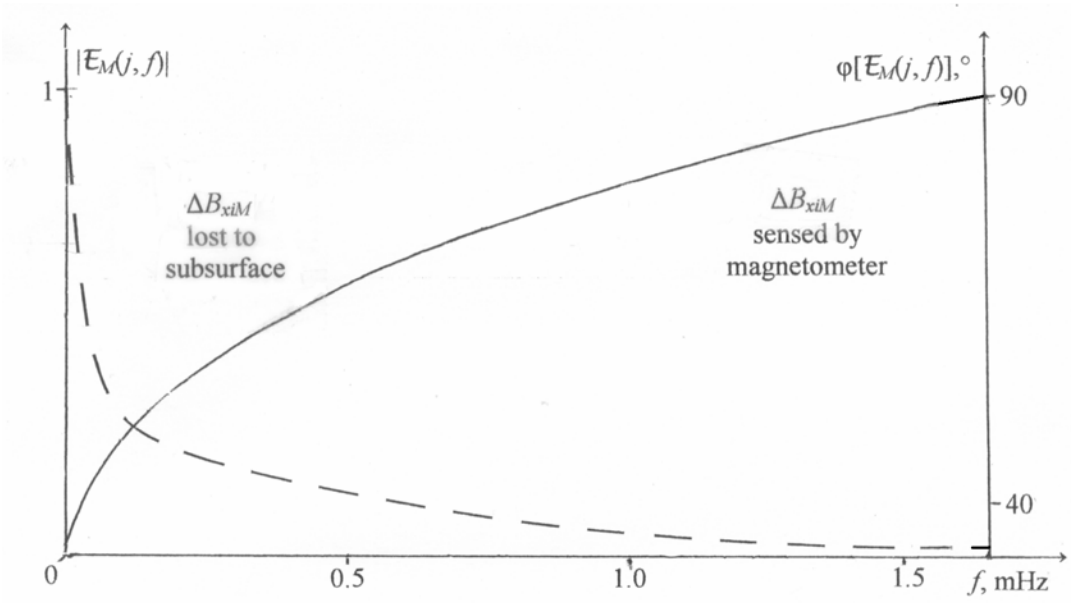

Figure 19. Amplitude (solid) and phase (dashed) spectral band of interest of the earth filter for Butler Bayou M.

The data of Figures 18 and 19 are smooth because they result from quadrature, a smoothing operation.

Figures 20 and 21 data result from the deconvolution of Figures 15 and 18 data. The interval of inflection shows up best in the real component of this isolated solution. Curvature of this function is described in Figure 22 with the selected frequency f_1 (the onset of zero/near zero curvature) also annotated. This is the lowest frequency limit for which (predictable) Alfven ionospheric electron movement dominates in the frequency band of maximum predictability. This is known because of the justification following Equations 25 and 26 and Figures 9 and 10. Figure 23 shows the very good logarithmic least squares fitting of the

phase spectrum which is apparently linear in this band. Evaluation of this function at f_1 completes the isolation solution. This is equation (22) truncated to $n = 1$.

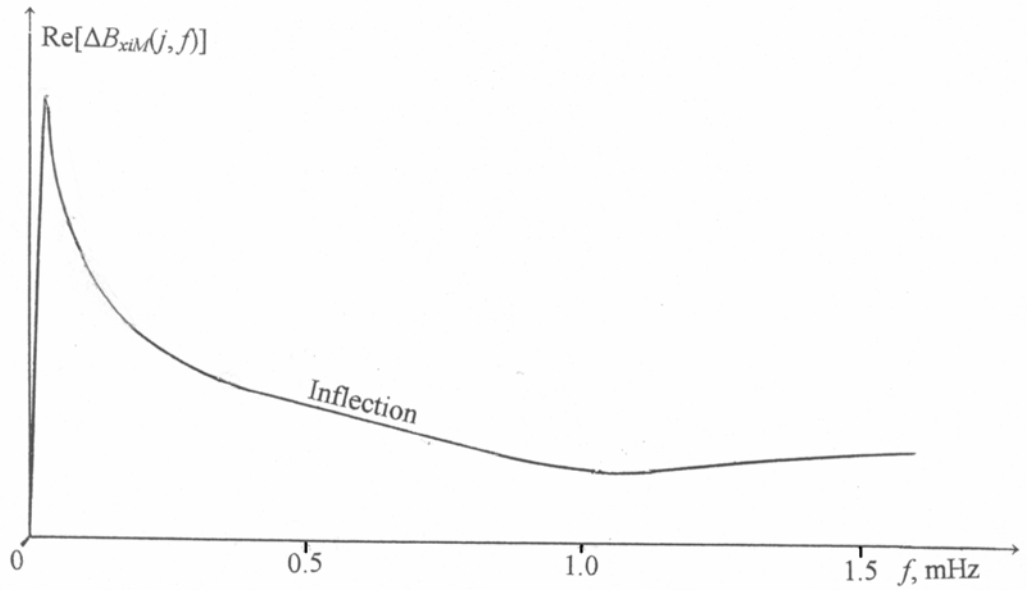

Figure 20. Real spectral band of interest of the isolated magnetic anomaly data signal for Butler Bayou M.

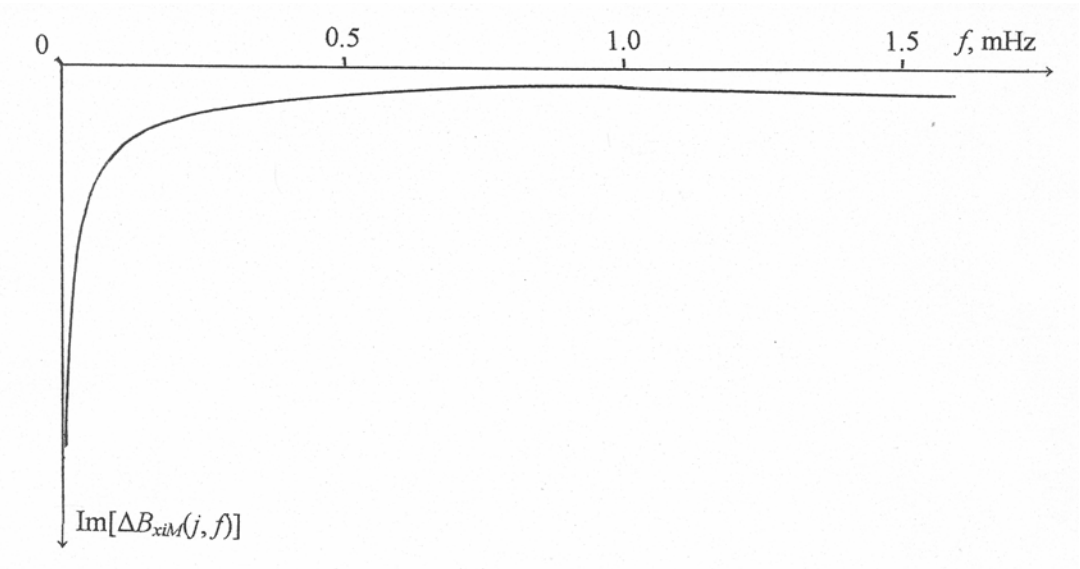

Figure 21. Imaginary spectral band of interest of the isolated magnetic anomaly data signal for Butler Bayou M.

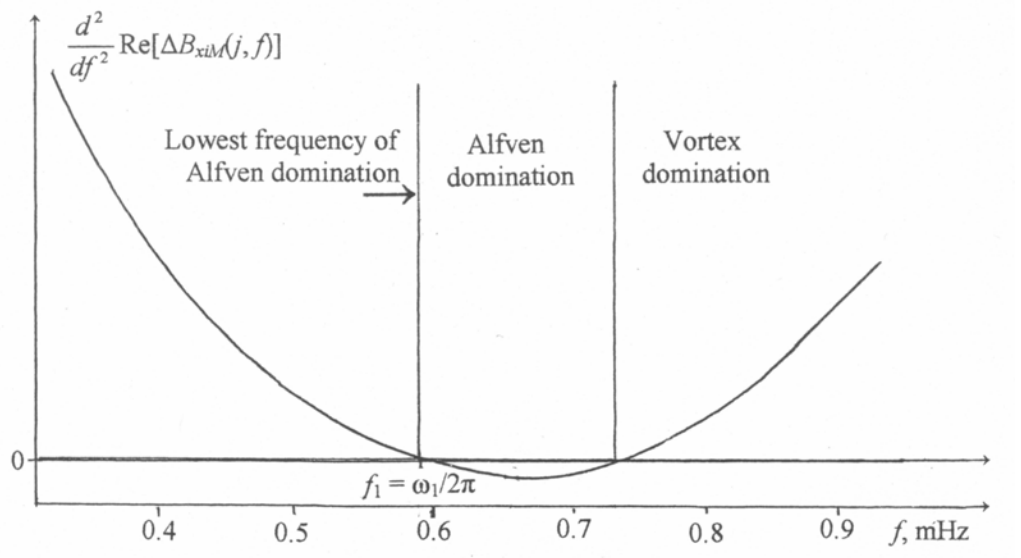

Figure 22. Real spectral curvature in the band of interest of the isolated magnetic anomaly data signal for Butler Bayou M.

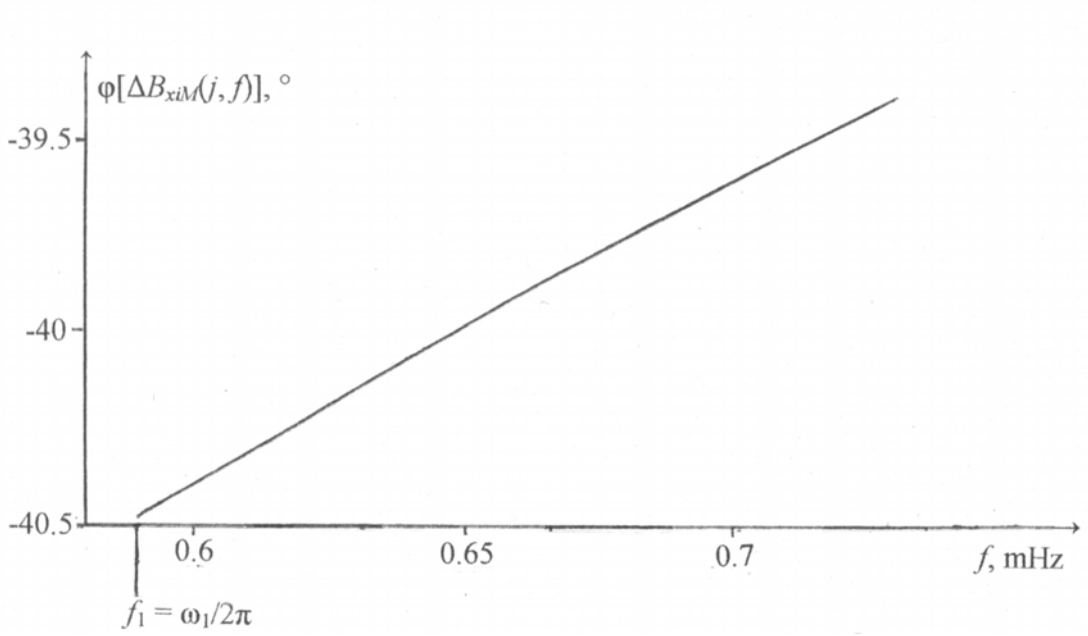

Figure 23. Phase spectra of the isolated magnetic anomaly data signal for the frequency band of Alfven domination for Butler Bayou M. The functions from equation (14) negation and the data fit from least squares coincide beyond human eye resolution to differentiate them.

The GPS data for evaluating the isolation begin with Figure 24. While only two SVs surround magnetometry point M, the ionospheric intersections of CORS-SV ranges (RF2Is) are azimuthally well distributed around M (Figure 25). These ranges and refracted range anomalies in the RF2Is become the observed arguments in equation (39) and its right hand side substitution into equation (40).

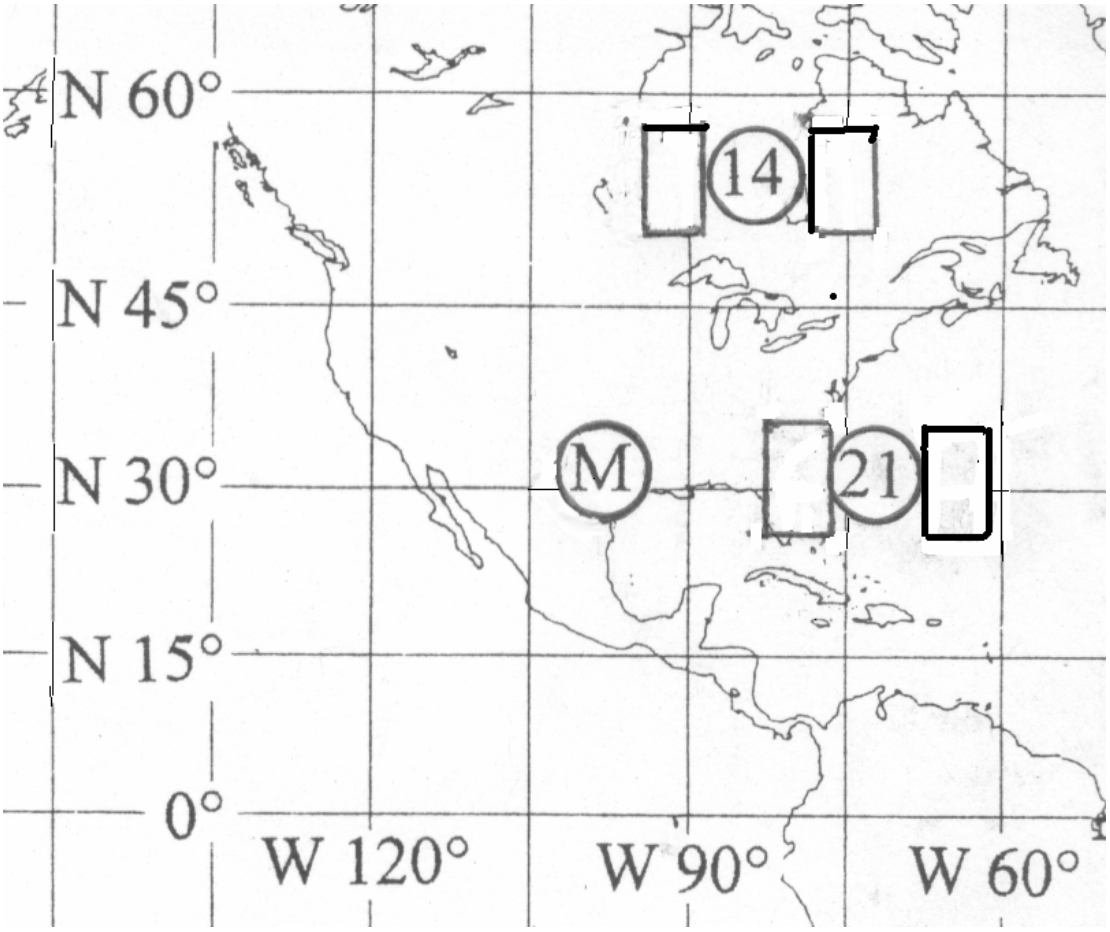

Figure 24. GPS SVs closest to the Butler Bayou M zenith on a *Snyder* [1987] base Mercator projection map, about midway through the September 25, 2002 observation. (Reprinted from a source with no copyright.)

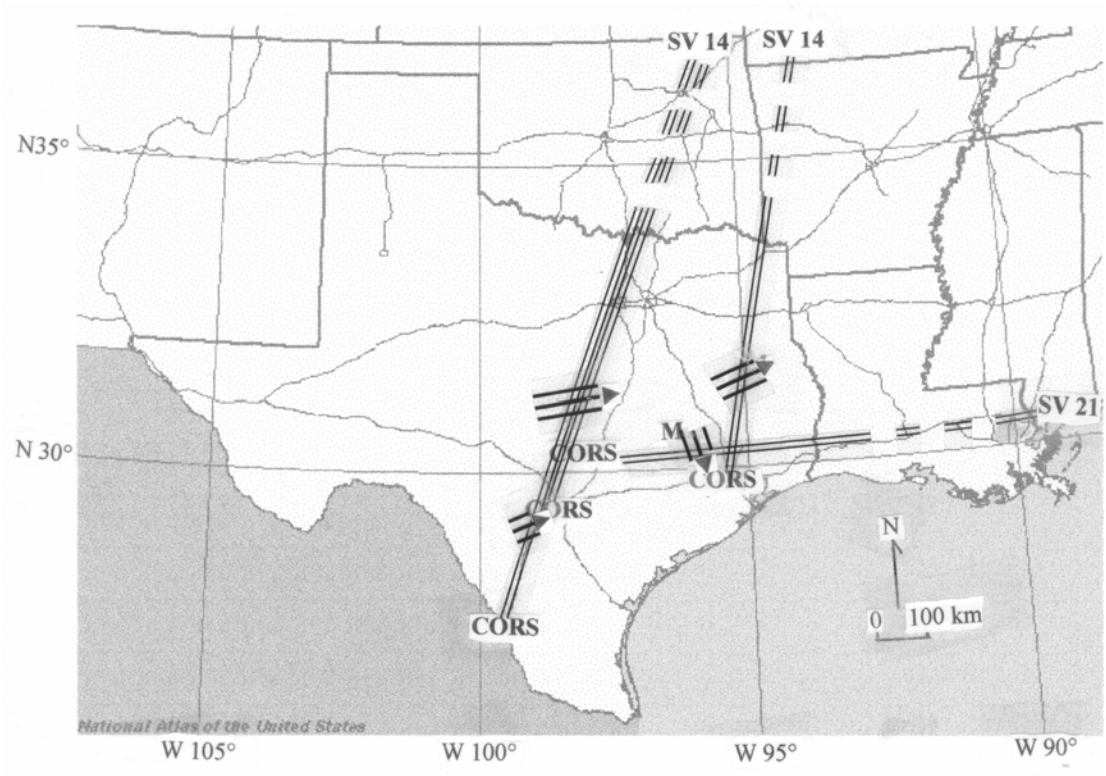

Figure 25. Texas and vicinity [*USGS*, 2004] GPS range portions (double lines) and RF2ISs (triple-lined arrows) around Butler Bayou M about midway through the September 25, 2002 observation. (Reprinted from a source with no copyright.)

Initially apparent in Figure 26 is the restoration of the low frequency content lost to the subsurface. (The rough $\Delta B_{xdwM}(t)$ becomes the smoother $\Delta B_{xiM}(t)$.)

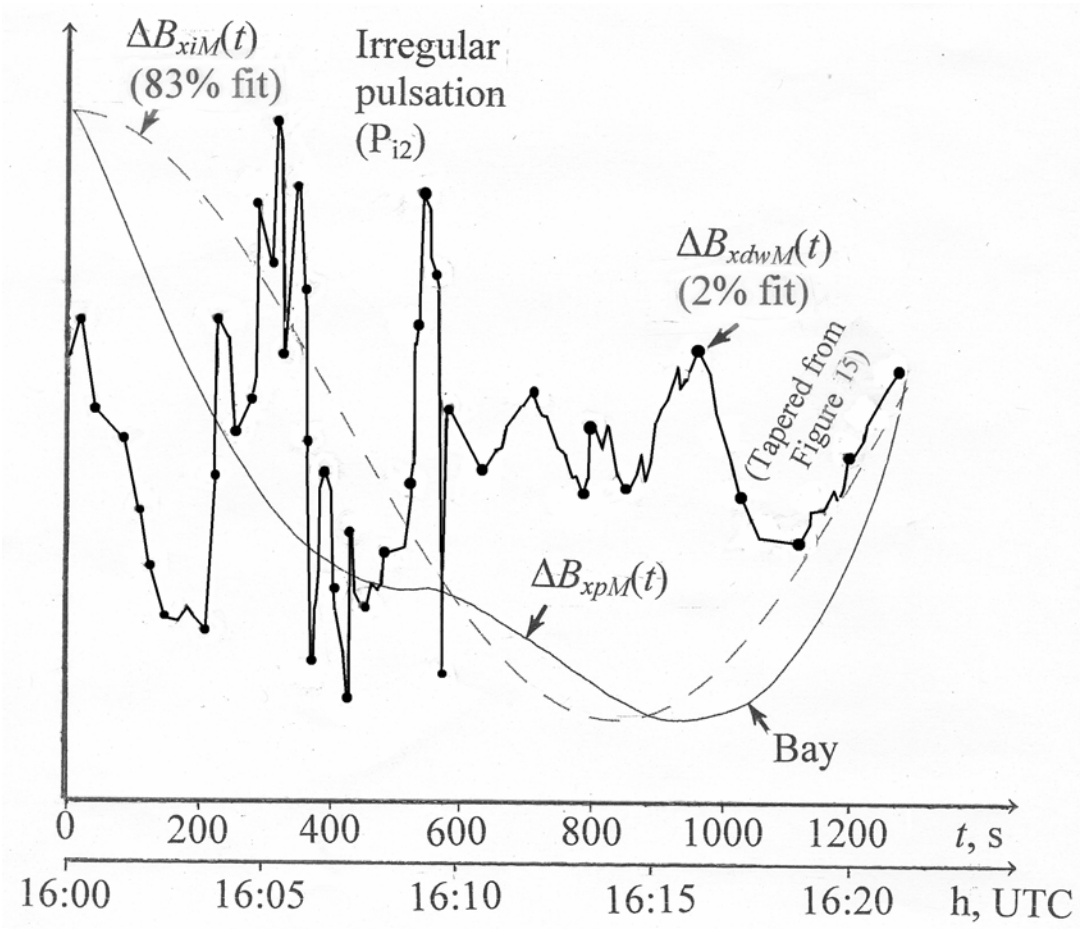

Figure 26. Comparison of the de-whorled (dotted), isolated (dashed), and pseudo- (solid) magnetic anomaly signals at Butler Bayou M on September 25, 2002. The ordinate axis is not labeled due to equation (41) proportionality only.

Over time t, the figure shows how use of subsurface conductivity data can dramatically improve estimation of a magnetic signal arising from ionospheric electron movement: from only 2% to 83%. The tapering (equalizing the first and last $\Delta B_{xdwM}(t)$ data to prevent Gibb phenomena in the Fourier transform) shown was done to prepare the Figure 15 de-whorled signal for Fourier transformation. At about 16:09 h, a certain higher frequency irregular pulsation (P_{i2}) [*McPherron*, 2002] is however evident in both the de-whorled and the pseudomagnetic curves. The $\Delta B_{xdwM}(t)$ irregular pulsation at about 16:05 h was probably too localized and too aliased by the RF2IS coverage to correlate with $\Delta B_{xpM}(t)$.

3.1.2. Crystalline Uplift: Enchanted Rock

Located along the inner margin of the Gulf Coastal Plain (Figure 27), the Enchanted Rock station ER occupies a point M upon an exposed granitic intrusion into carbonate country rock. Figure 28 shows the conductivities of the region, much more electrically resistive than those underlying Butler Bayou.

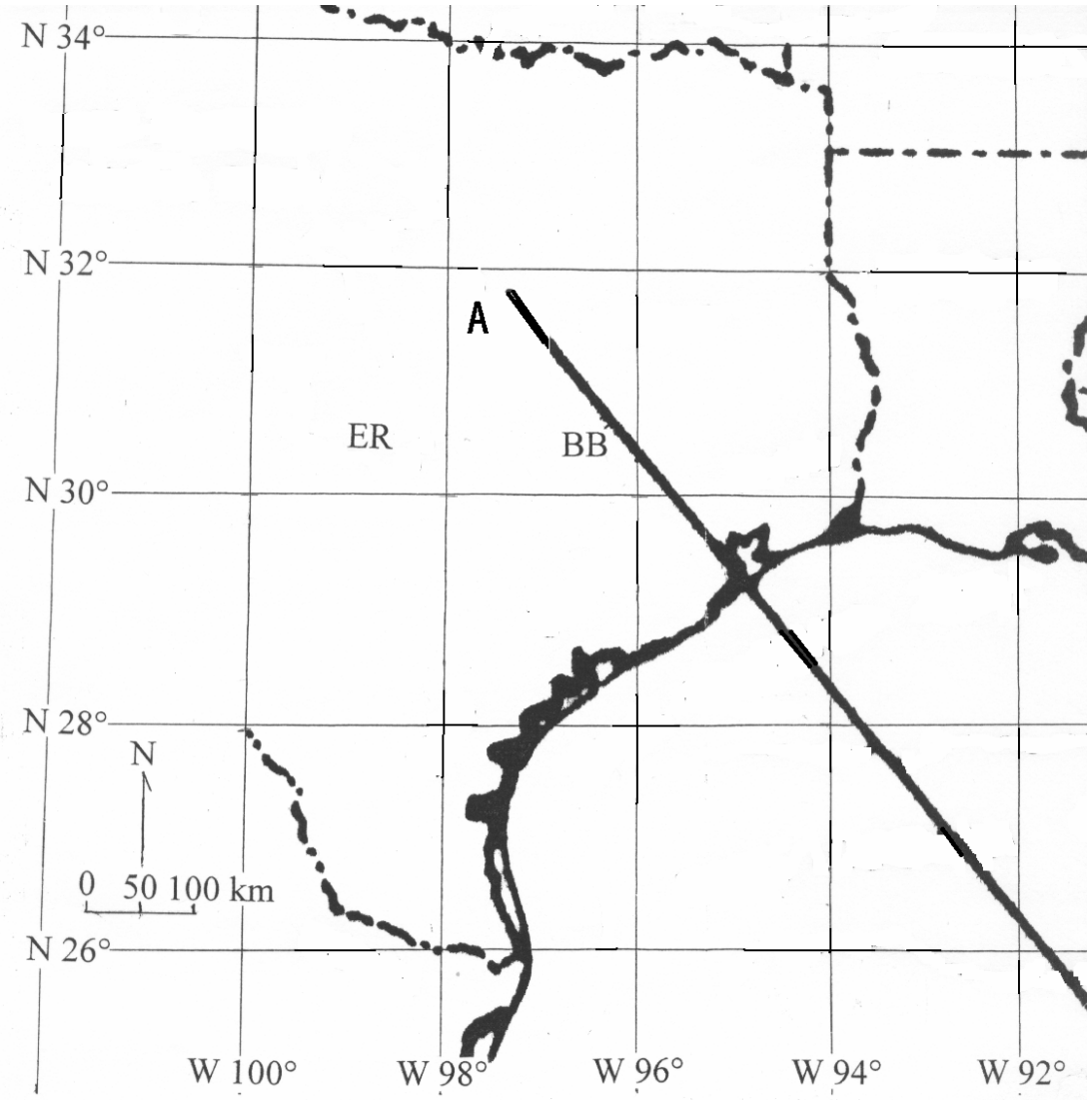

Figure 27. Geographic and geologic setting of the Enchanted Rock (ER) study station. (Reprinted with permission from *The Geology of North America; An Overview, D. M. Worrall and S. Snelson,* 1989, Geological Society of America, Boulder, CO, 1989, Geological Society of America.) United States Geological Survey (USGS) "Enchanted Rock" and "Crabapple" 7.5 minute topographic quadrangles, 1967 (no copyrights). *Renfro et al.* [1973] geologic map published by the American Association of Petroleum Geologists (AAPG) is AAPG©[1973] and reprinted by permission of the AAPG whose permission is required for further use.

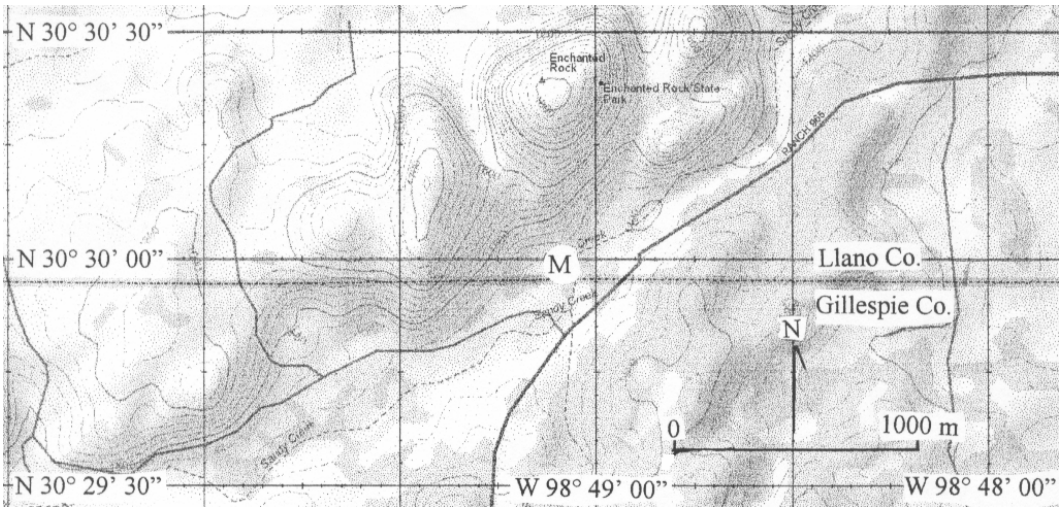

Figure 27. Continued.

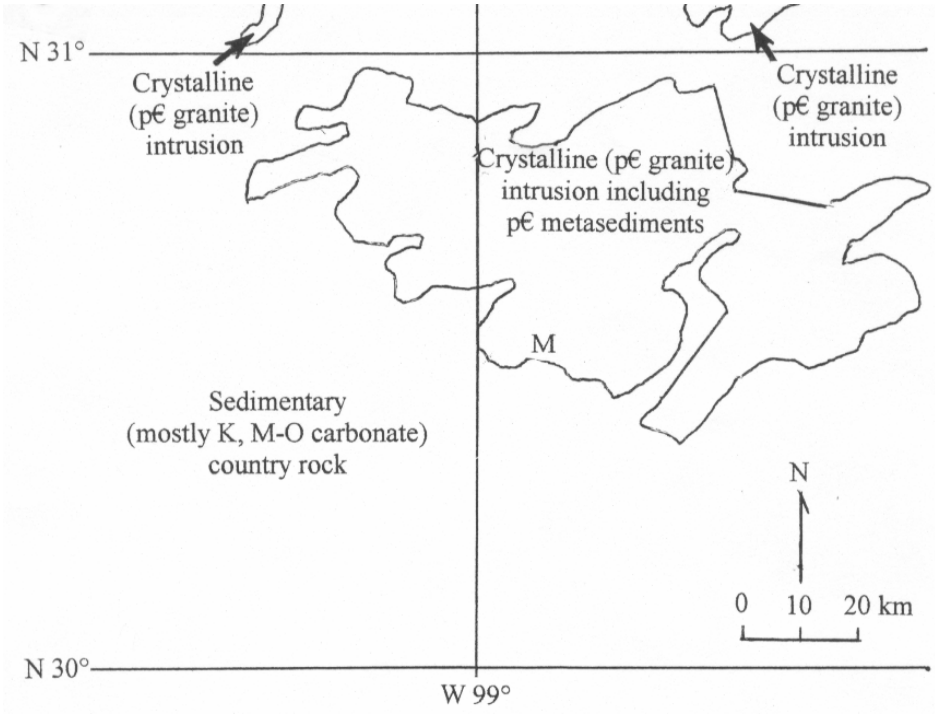

Figure 27. Continued.

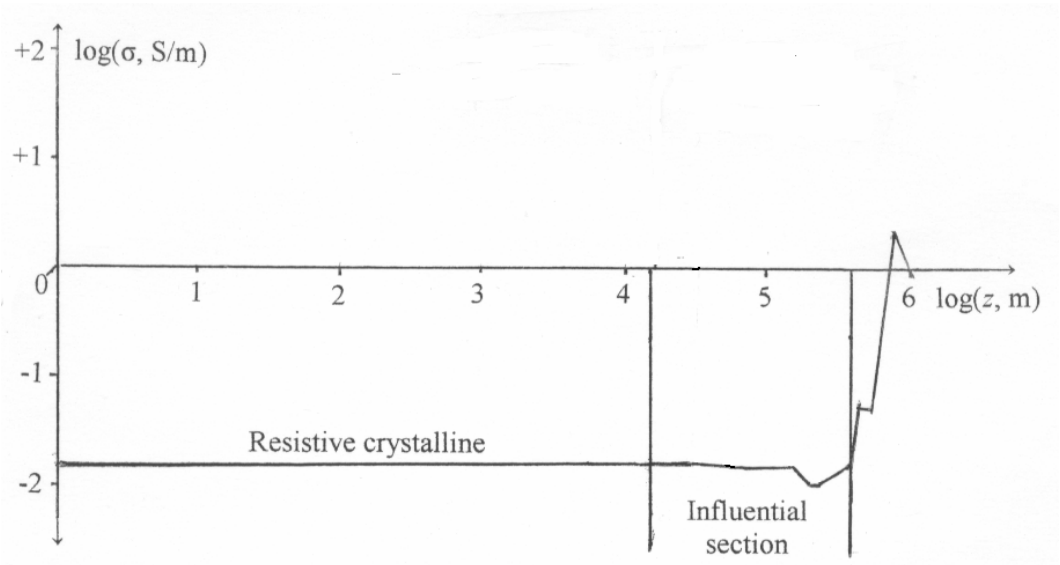

Figure 28. Assumed Enchanted Rock conductivity profile [*Lizarralde et al.,* 1995]. Data are from a long period magnetotelluric survey at Carty Lake, Ontario.

Figure 29 shows the observed magnetic data (with a sample interval of 10 s). The trend is much less pronounced than for Butler Bayou in Figure 14 because the resistivity has kept the low frequencies intact. (Not as many of them have been lost to the subsurface.) The same is true for the de-whorled data of Figure 30.

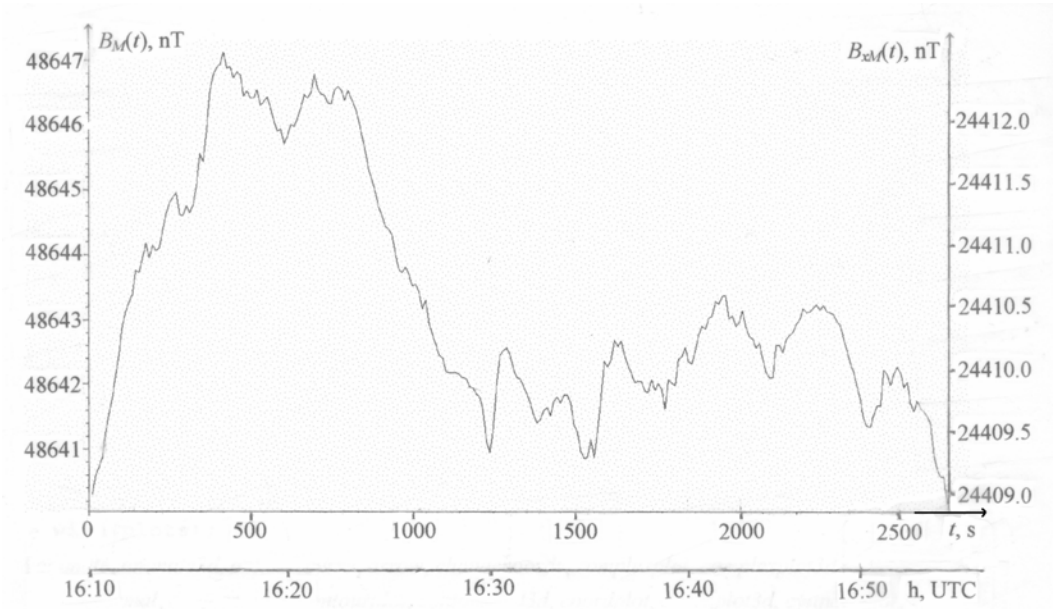

Figure 29. Observed magnetic data anomaly signal at Enchanted Rock M. The 90% confidence error is approximately ±0.01 nT .

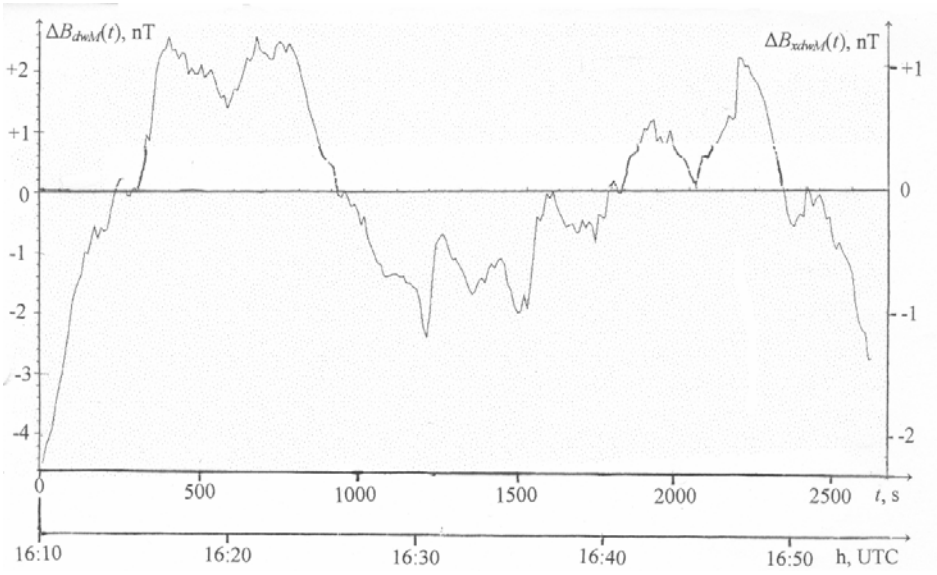

Figure 30. De-whorled magnetic anomaly data signal and its north component at Enchanted Rock M.

Like Figure 16, Figure 31 shows the amplitude spectrum and an empirical continuum from zero to the Nyquist frequency. The Enchanted Rock phase spectrum is also randomly trivial (composed of many noise-resembling $\tan^{-1}$ functions) and therefore omitted.

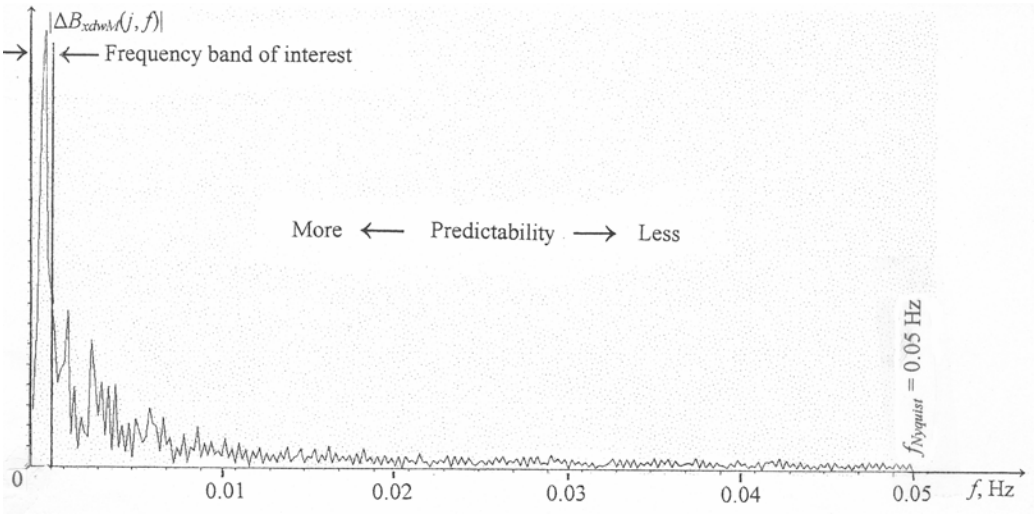

Figure 31. Amplitude spectrum (to the Nyquist frequency) of the de-whorled magnetic anomaly data signal at Enchanted Rock M.

On a frequency band of maximum predictability the same as that for Butler Bayou, Figure 32 includes the phase spectrum. The application of equations (4) and (7) on the data of Figure 28 produce the amplitude and phase spectra of Figure 33: the earth filter at depth (right below the influential section). Equation (9) then expresses the earth filter at the magnetometer, Figure 34.

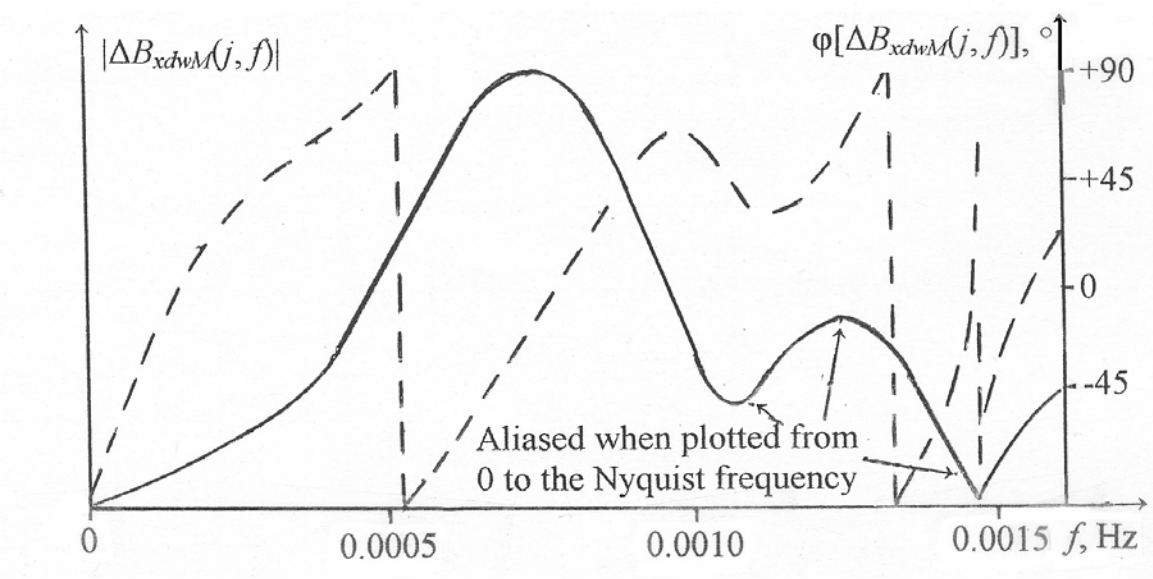

Figure 32. Amplitude **(**solid) and phase (dashed) spectral band of interest of the de-whorled magnetic anomaly data signal at Enchanted Rock M.

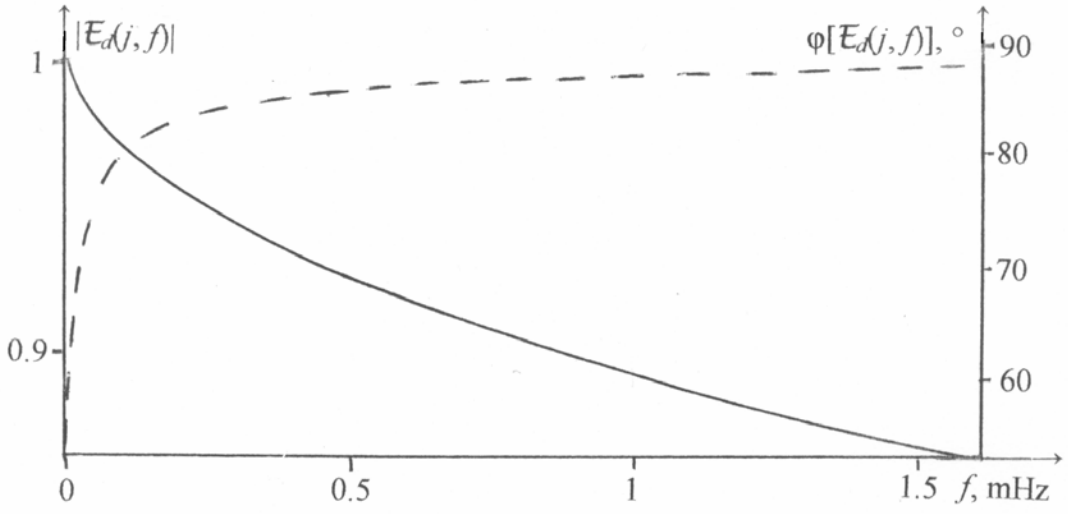

Figure 33. Amplitude (solid) and phase (dashed) spectral band of interest of the earth filter at the base of the influential section beneath Enchanted Rock M.

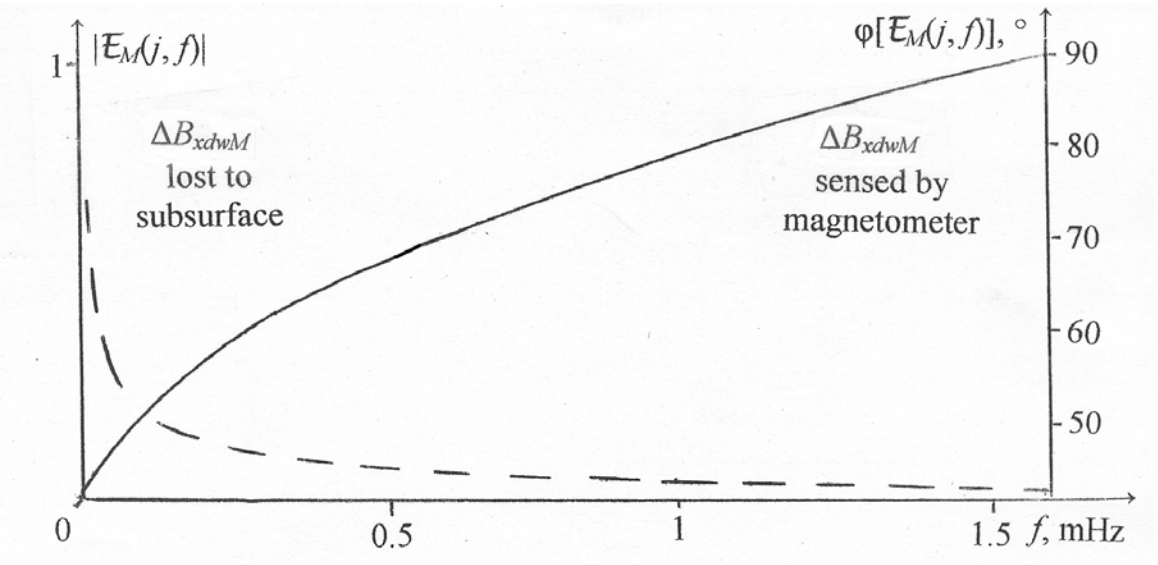

Figure 34. Amplitude (solid) and phase (dashed) spectral band of interest of the earth filter at Enchanted Rock M.

Deconvolution of Figures 30 and 34 data gives the curves in Figures 35 and 36.

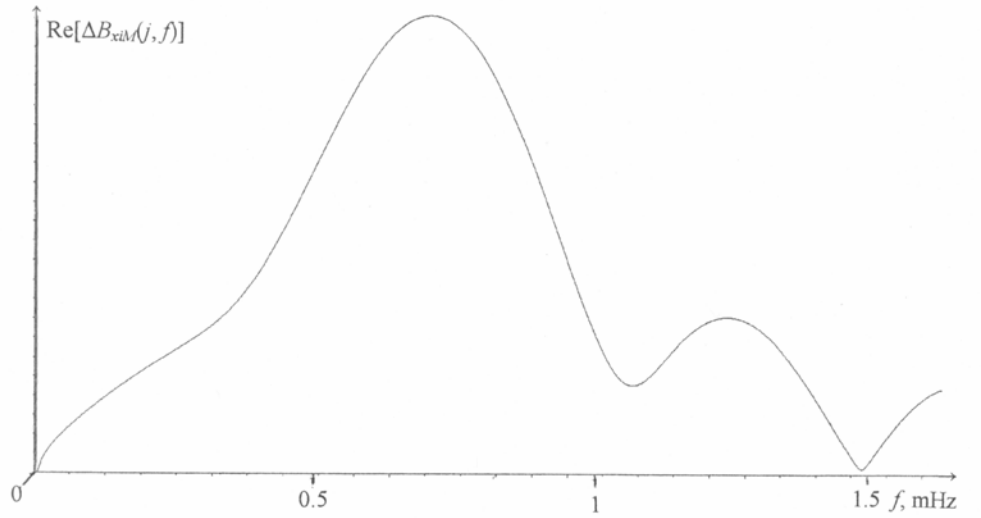

Figure 35. Real spectral band of interest of the isolated magnetic anomaly data signal for Enchanted Rock M.

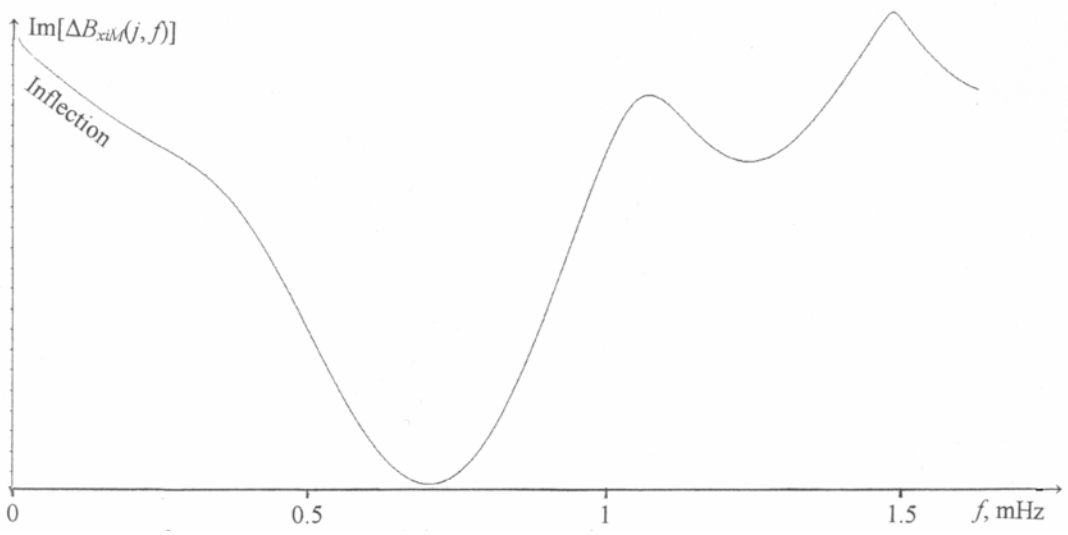

Figure 36. Imaginary spectral band of interest of the isolated magnetic anomaly data signal for Enchanted Rock M.

For this time and field station, the interval of inflection shows up best in the imaginary component of this isolated solution. Curvature of this function is described in Figure 37 with the selected frequency f_1 included in the annotation. This is the lowest frequency limit of any zero or near zero curvature where Alfven

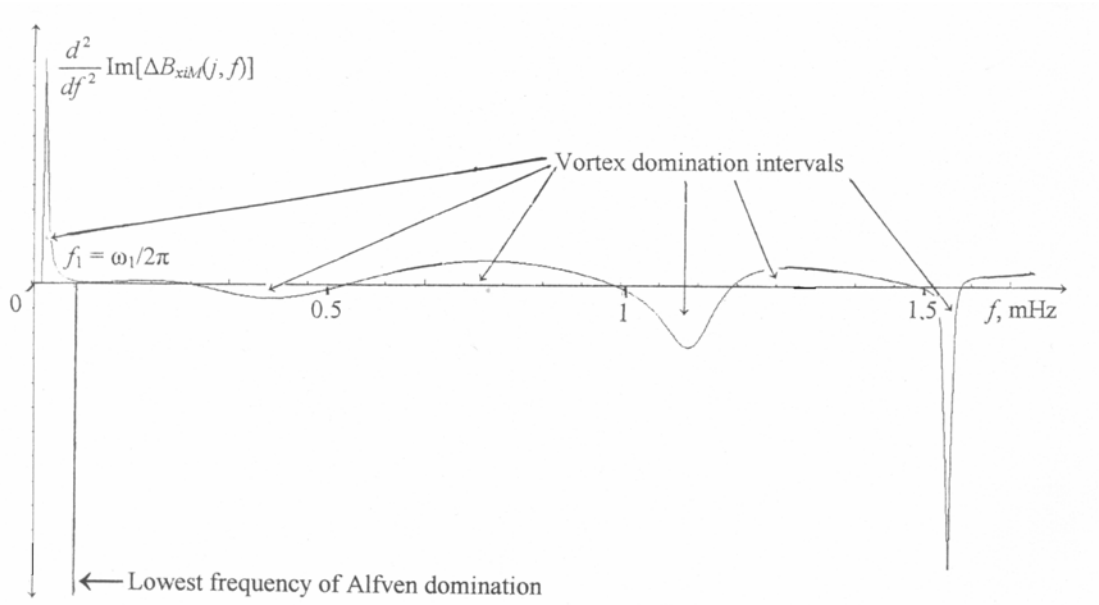

Figure 37. Imaginary spectral curvature in the band of interest of the isolated magnetic anomaly data signal for Enchanted Rock M.

ionospheric electron movement dominates in the frequency band of maximum predictability. Figure 38 shows the logarithmic least squares fitting of the phase function. Evaluation of this function at f_1 completes the isolation solution when substituted into equation (22) and truncated to $n = 1$.

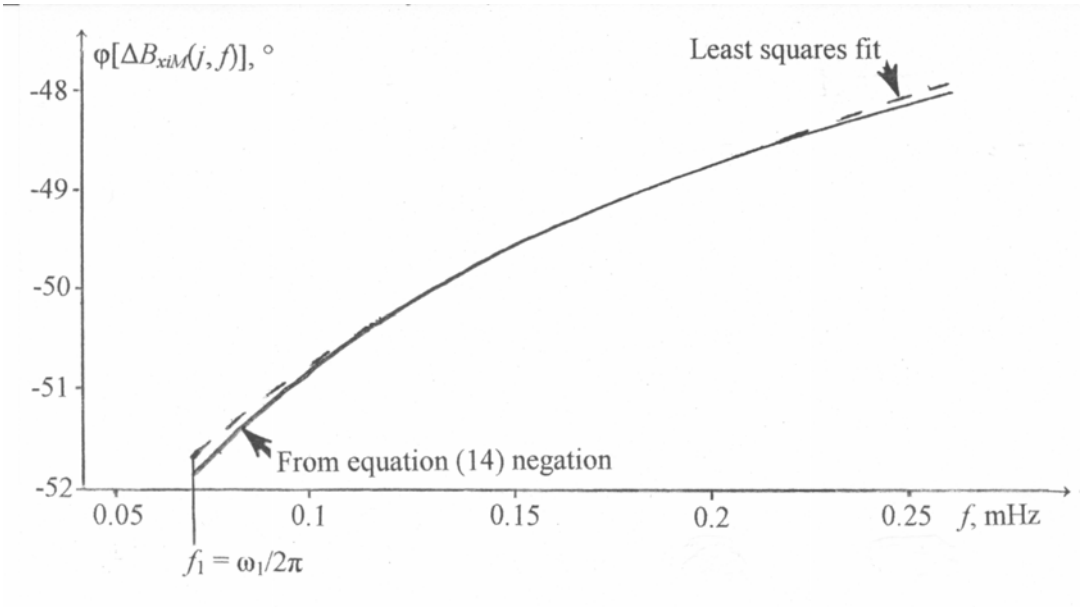

Figure 38. Phase spectra of the isolated magnetic anomaly signal for the frequency band of Alfven domination for Enchanted Rock M.

The GPS data for evaluating the Enchanted Rock isolation begin with Figure 39. Four SVs now surround magnetometry point M. The ionospheric

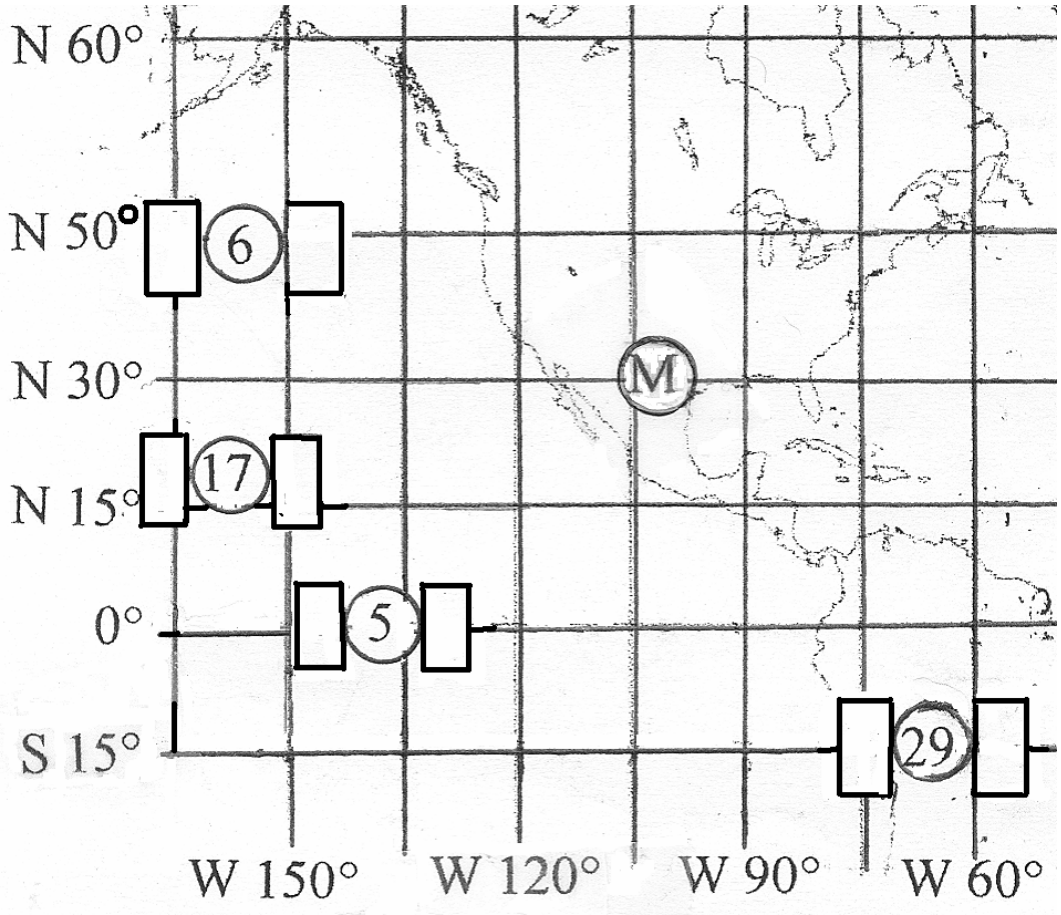

Figure 39. GPS SVs for Enchanted Rock M selected for maximum RF2I azimuthal coverage on a *Snyder* [1987] Mercator projection, about midway through the May 28, 2003 observation. (Reprinted from a source with no copyright.)

RF2Is are also azimuthally well distributed around M (Figure 40). These ranges and refracted range anomalies in the RF2Is become the observed arguments in equation (39)

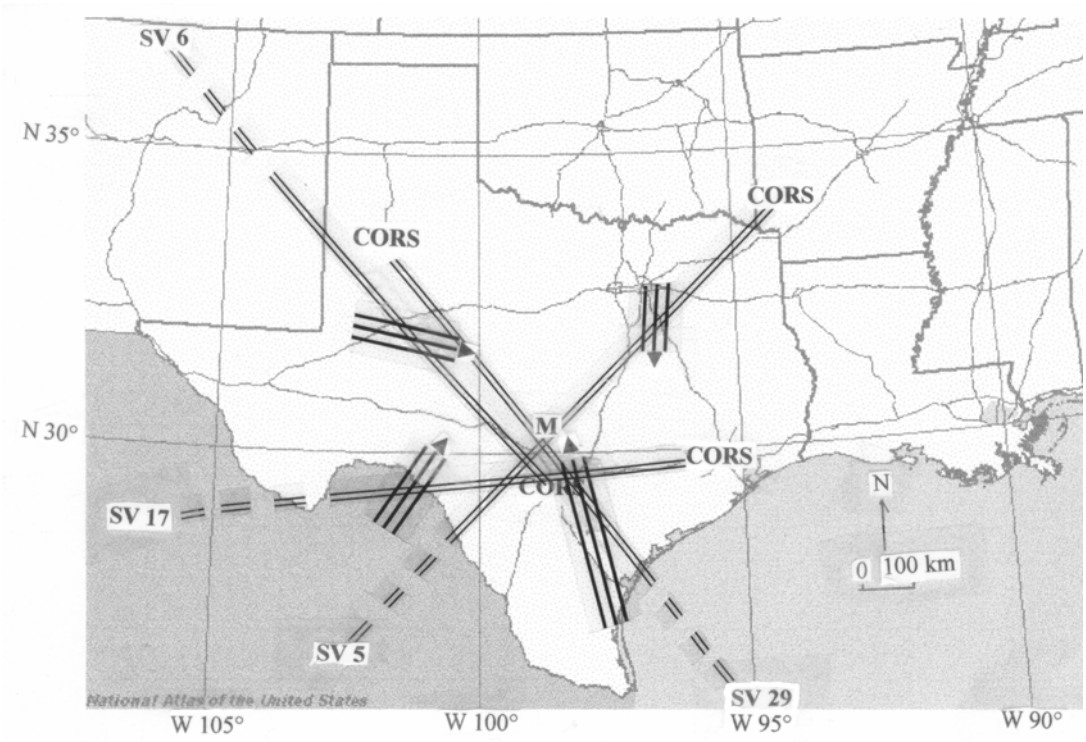

Figure 40. Texas and vicinity [*USGS*, 2004] showing GPS range portions (double lines) and RF2ISs (triple-lined arrows) around Enchanted Rock M about midway through the May 28, 2003 observation. (Reprinted from a source with no copyright.)

and its right hand side substitution into equation (40).

The restoration of the lowest frequency magnetic anomaly content lost to the subsurface is also notable in Figure 41, albeit less than for Butler Bayou. Probably due to more SVs being used, the figure better shows how use of subsurface conductivity data can improve estimation of a magnetic signal arising

from ionospheric electron movement; now from 2% to 96%. Pre-Fourier transformation tapering for the de-whorled anomaly is also shown in Figure 41. At about 16:45 h, another higher frequency irregular pulsation (P_{i2}) (*McPherron*, 2002) is however evident in both the de-whorled and the pseudomagnetic signals.

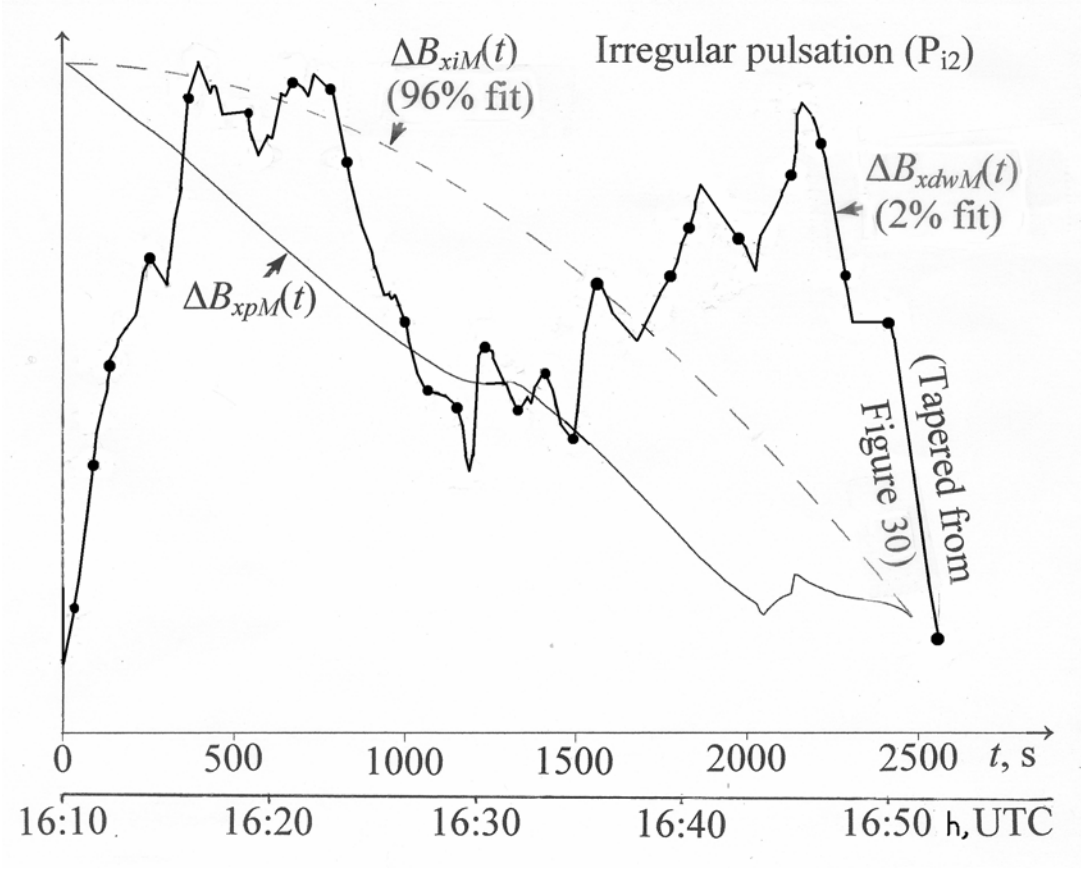

Figure 41. Comparison of the de-whorled (dotted), isolated (dashed), and pseudo- (solid) magnetic anomaly data signal at Enchanted Rock M on May 28, 2003.

3.2 Repeated Results

Both stations M were revisited. These second surveys were of the same durations and sample intervals as their initial measurements. The only differences were that three and not four ranges were used in the correlations. Also, only the most important result figures are shown for each. These are the observed magnetic anomaly data signal, the de-whorled magnetic anomaly data signal, the spectral curvature, and the comparisons with the pseudomagnetic data signal.

3.2.1 Sedimentary Basin: Butler Bayou

Figure 42 shows a strong cubic polynomial for the diurnal and whorl components of the observed data anomaly signal.

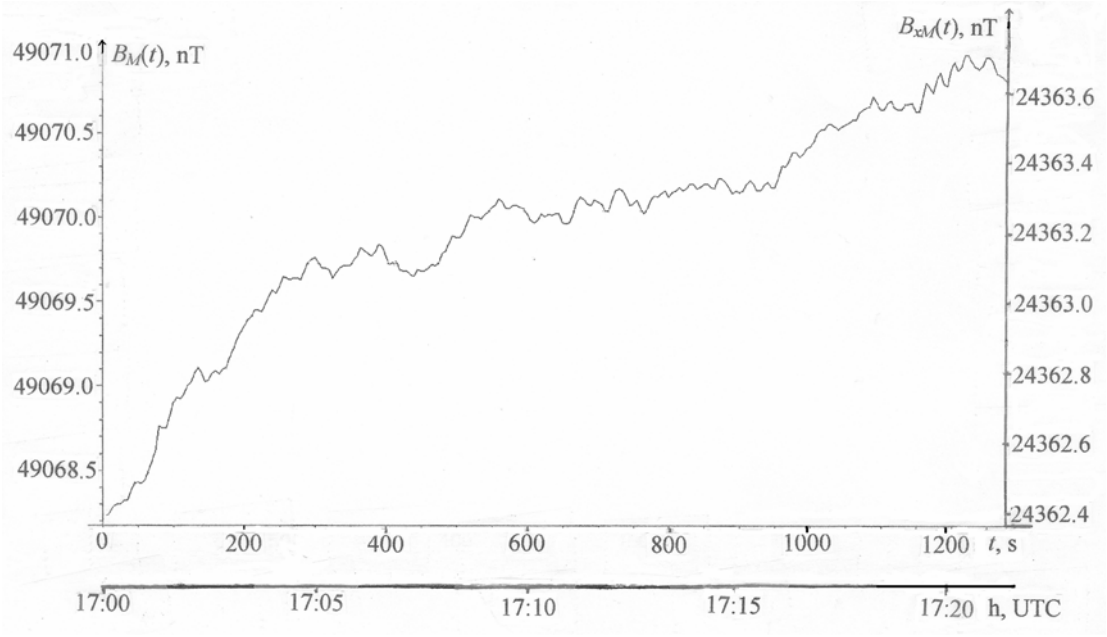

Figure 42. Repeated observed magnetic anomaly data signal at Butler Bayou M.

Because of this, the de-whorled signal (Figure 43) is very stationary and has very little curvature, meaning that what vortex domination that is present is not very pronounced.

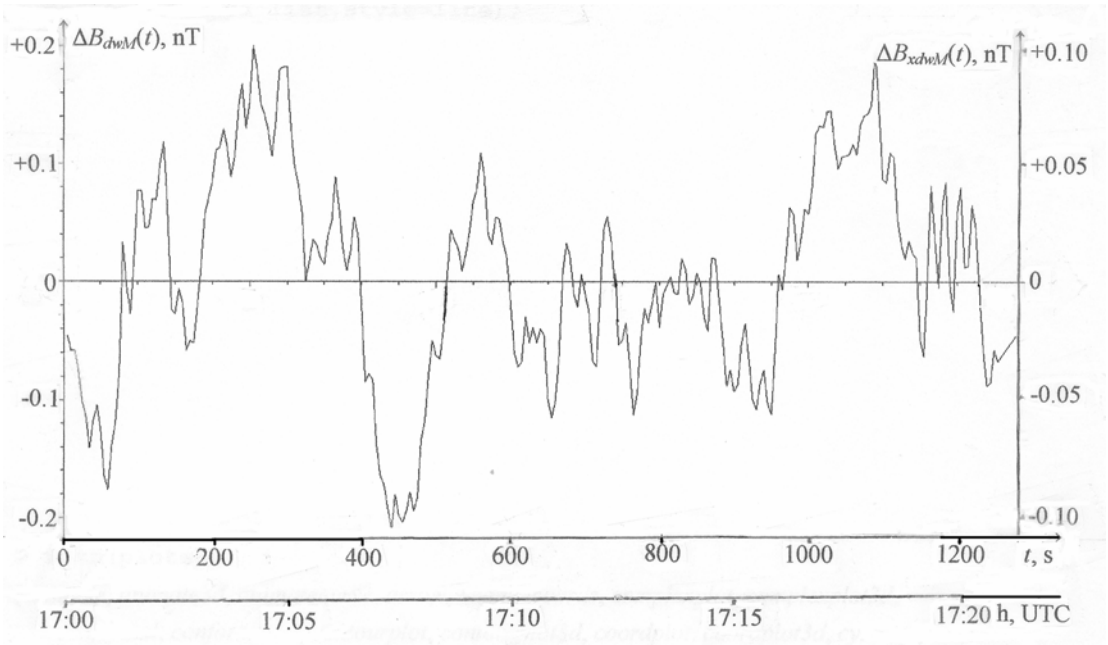

Figure 43. Repeated de-whorled magnetic anomaly data signal and its north component at Butler Bayou M. The signal has been minimally tapered to prevent Gibb phenomena in later Fourier transformation.

Consequentially, Figure 44 has only two notable departures from zero curvature. The abscissa of the local minimum nearest this level is interpreted to be the lowest frequency of Alfven domination.

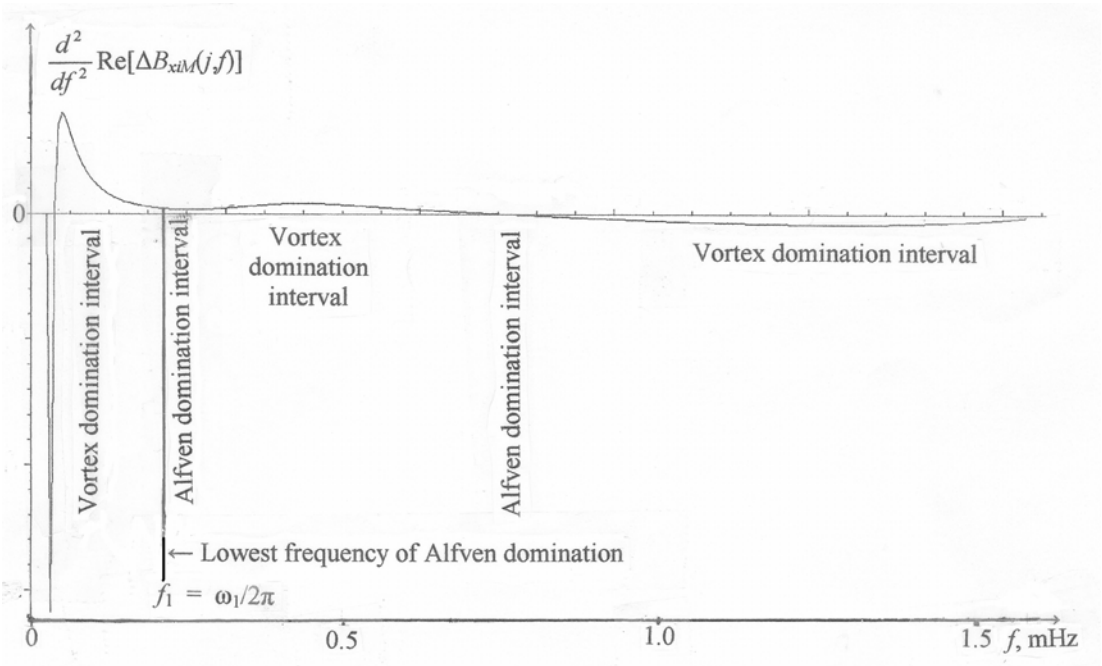

Figure 44. Repeated real spectral curvature in the band of interest of the isolated magnetic anomaly data signal for Butler Bayou M.

The isolation is still a good one, however, as shown in Figure 45.

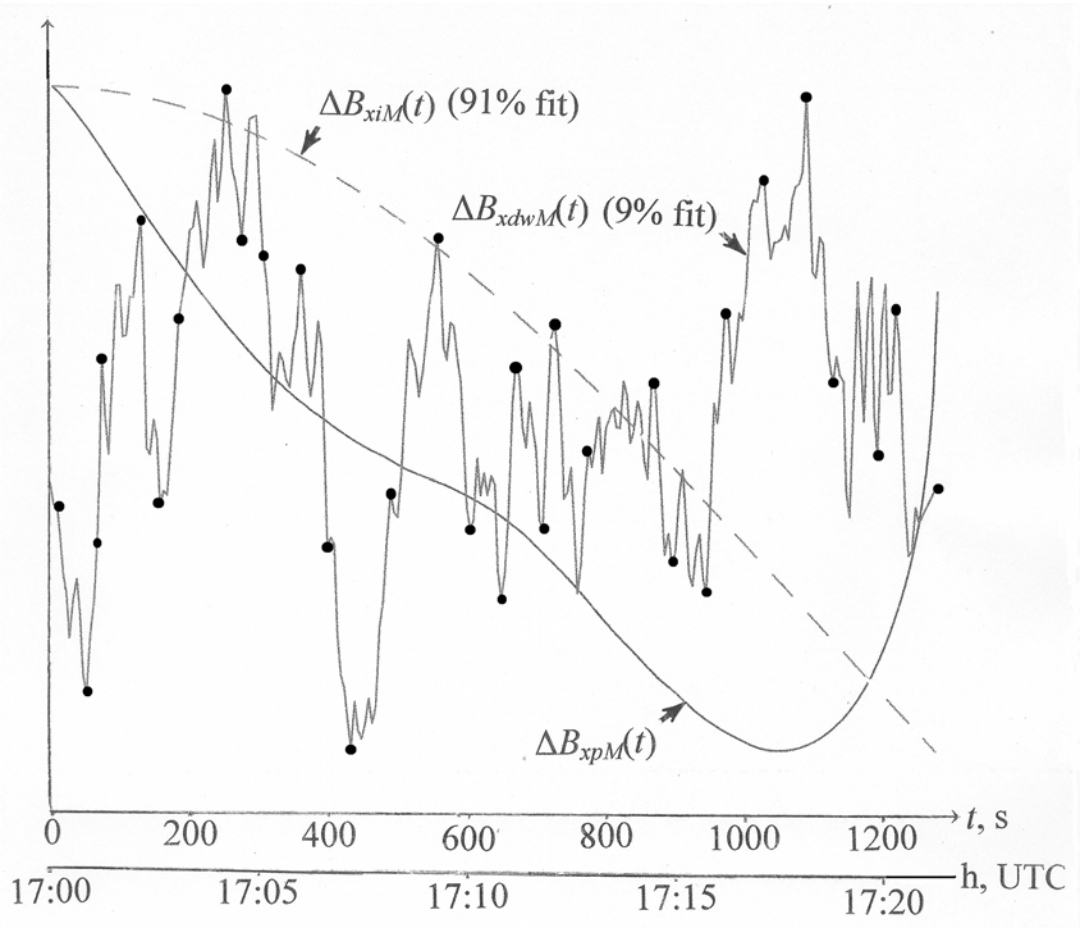

Figure 45. Repeated comparison of the de-whorled (dotted), isolated (dashed), and pseudo- (solid) magnetic anomaly signals at Butler Bayou M on April 15, 2004.

3.2.2 Crystalline Uplift: Enchanted Rock

Figure 46 depicts the observed magnetic anomaly data signal for the Enchanted Rock repetition. The trend is again less pronounced since lower frequency whorls are left relatively intact by the resistive bedrock.

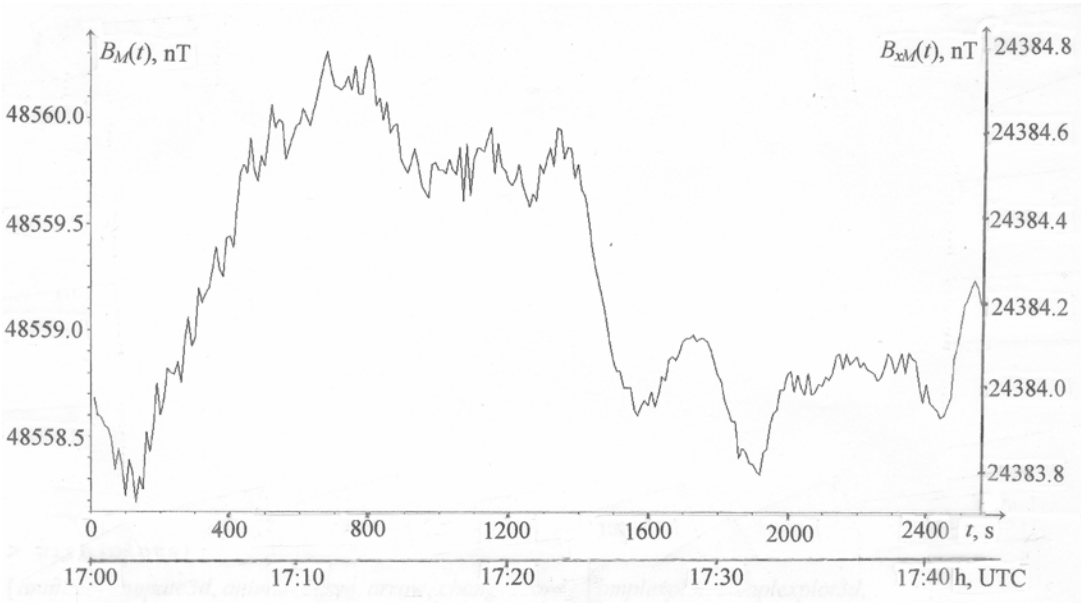

Figure 46. Repeated observed magnetic anomaly data signal at Enchanted Rock M.

Upon comparison to the Butler Bayou repetition, somewhat more curvature is shown in the de-whorled Figure 47.

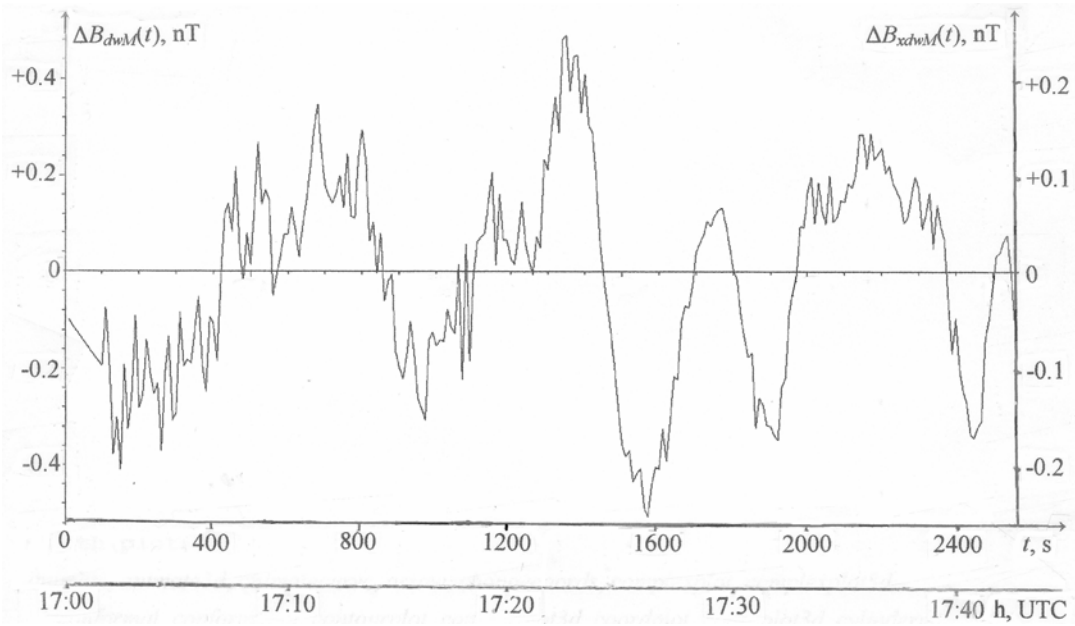

Figure 47. Repeated de-whorled magnetic anomaly data signal and its north component at Enchanted Rock M. The signal has been tapered to prevent Gibb phenomenon in later Fourier transformation.

This causes more amplitude difference between the Alfven and vortex domination intervals in the curvature plot Figure 48.

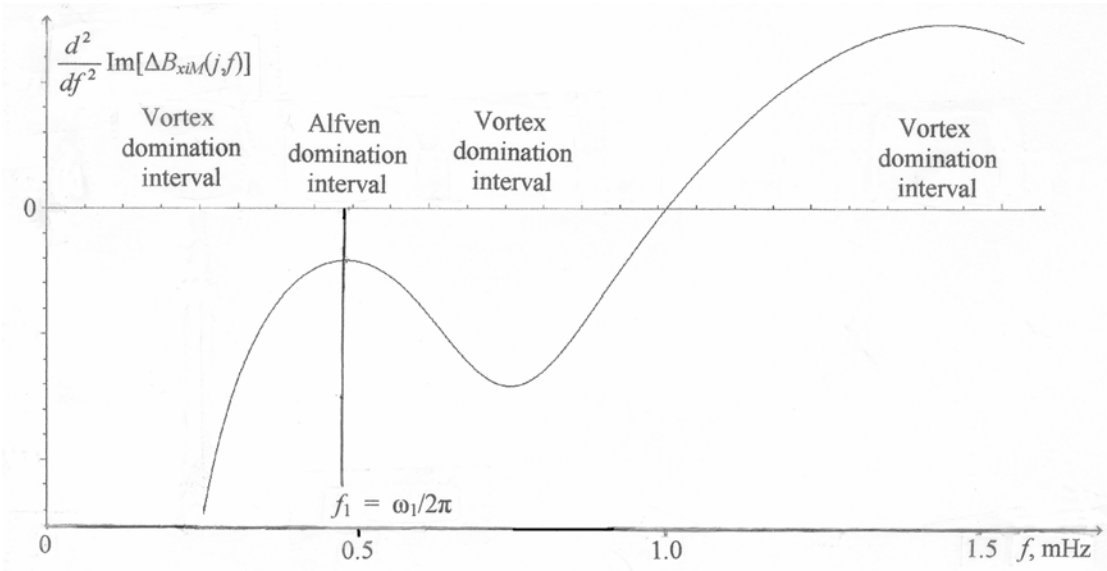

Figure 48. Repeated imaginary spectral curvature in the band of interest of the isolated magnetic anomaly data signal for Enchanted Rock M.

Application of the selected frequency f_1 and its corresponding phase (not shown) improves the de-whorled anomaly data signal correlation with the pseudomagnetic anomaly signal as shown in Figure 49.

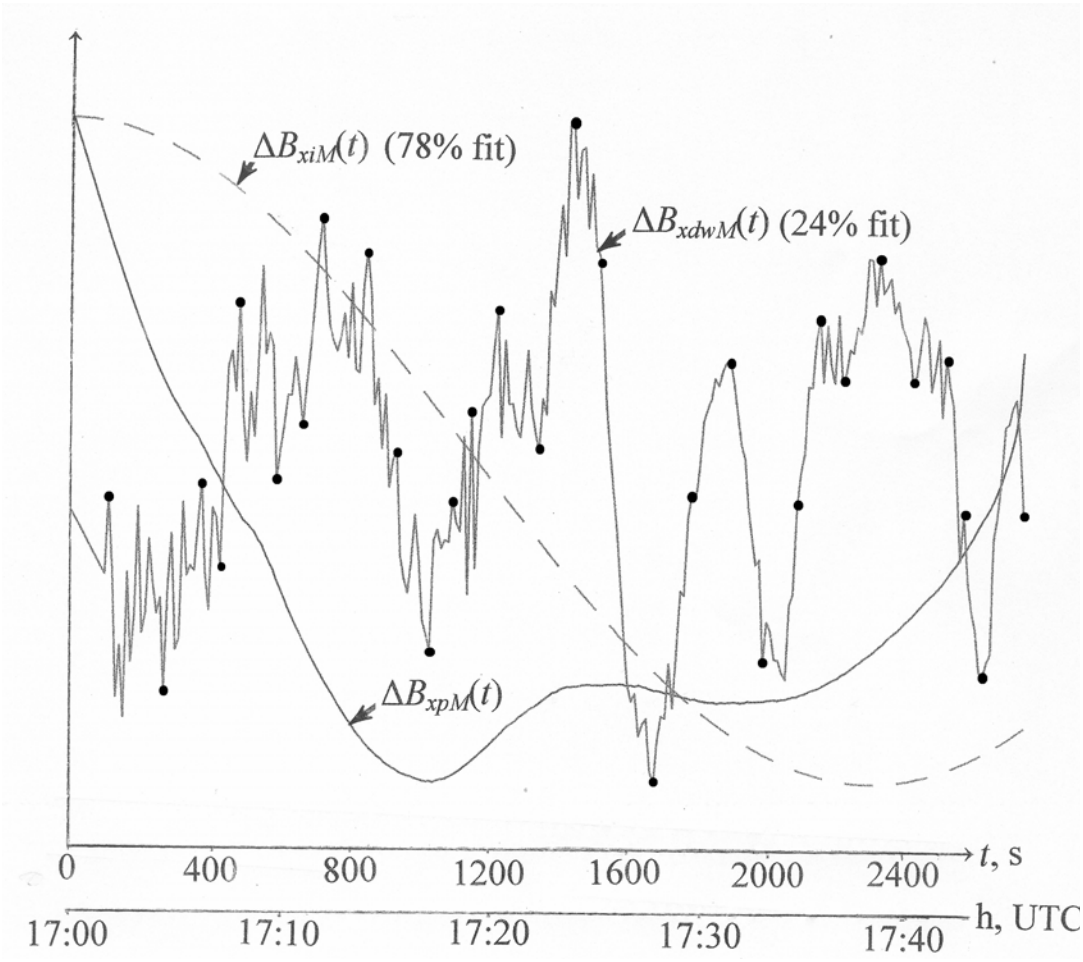

Figure 49. Repeated comparison of the de-whorled (dotted), isolated (dashed), and pseudo- (solid) magnetic anomaly signals at Enchanted Rock M on April 21, 2004.

4. DISCUSSION

Three major principles stand out from the SCIRCMS results. Electromagnetic wave propagation to diffusion at the topography results in loss of the lower frequency content of the incident energy to the subsurface. When the subsurface conductivity is known, forward modeling of the diffusive earth filter effects can be used to account for and restore this energy. As an evaluation of the restoration, abbreviated Biot-Savart modeling of ionospheric electron movement can correlate much better with the signal of the energy than without the restoration. SCIRCMS is not without its exceptions and limitations. *Vozoff* [1972] advises the possibility of non-horizontally-polarized and non-plane-wave magnetic energy. The horizontal vortex ionospheric electron type movement [*Spaulding*, 1995] may greatly dominate over that of the Alfven [*McPherron*, 2002] type either above or between formations. Also at these interfaces, *Telford et al*. [1982] mention the possibility that magnetic permeability may significantly change. Concerning the entire spatiotemporal extent of the SCIRCMS model, a non-linear system for the geoelectric model of the earth in this space-time domain may be more suitable. There may be anisotropy of the subsurface conductivity [*Ward and Hohmann*, 1987]. There may be structure in or near the influential section more analytical by two- [*Jones and Price*, 1971] or three- [*Weiss and Everett*, 1996] dimensional methods. The simultaneous signals

acquisition and processing parameters could be incompatible with the vortex-Alfven domination demarcation band. Only a spherical earth model has been used so far. The improvements to the shortcomings are rarely applicable and insignificant, with the probable exception of using more SVs near M. The subsurface conductivity models for Butler Bayou and Enchanted Rock are probably accurate to approximately ± 0.009 S/m. Errors in these quantities in excess of about ± 0.015 S/m would probably critically discredit the low frequency component restoration process.

In comparison with previous publications, SCIRCMS considerably improves on the geomagnetic model used by *Bassiri and Hajj* [1993]. This is because restoration of magnetic intensity lost to the subsurface gives a magnitude that can be upward continued to cause a more accurate ionospheric magnetic intensity for their aeronomy. SCIRCMS also makes a refraction capability description of more common ionospheric events beyond the *Afraimovich* [2000] solar flare response detection only: magnetic intensity signals in conjunction with electron density monitoring give better refractivity control.

Four academic improvements to SCIRCMS would be worthwhile. The most important of these would be showing how the low frequency magnetic anomaly signal content can also be restored from loss of both two- and three-dimensional subsurface structure. Stationarity and ergodicity tests of the spectral components of the magnetic signal observed at the surface could be

done. Kalman filtering for RF2IS data with states to include SV positions and their time derivatives would be valuable, especially for real time aeronomic modeling. Perhaps more trivially, exploitation of the zero and near zero curvature bands (truncating equation (22) to $n = 2$ or $n = 3$) would improve the correlations. The Enchanted Rock repeated analysis would also have had a higher correlation with the pseudomagnetic anomaly data signal if the magnetometry was done in the presence of less unpredictable cultural noise.

Industrially, SCIRCMS systematic accounting of the diffusion effects of conductivity under magnetic observatories could augment global ionospheric tomography models. This would be much less expensive than present ionospheric tomography methods which employ rocket-launched hardware. This in turn could improve magnetic field and electron density control in the ionosphere to aid the solution of many aeronomic problems that arise in navigation, guidance, communications, meteorology, and ancillary developments.

5. CONCLUSION

SCIRCMS has reasonably isolated terrestrially-observed magnetic signals by restoration of their content diffusively lost to the subsurface. This isolation has made processed anomalies in these signals correlative with appropriately processed anomalies in GPS range data. The isolation processing includes electromagnetic modeling of the earth as a linear system and estimation of the attenuating effects of a one-dimensional subsurface. The GPS range processing is a derived application of the Biot-Savart law.

The method has been tested over both a relatively electrically-conductive sedimentary basin and a relatively electrically-resistant igneous intrusion. Respective correlation results of 83%, 96%, 91%, and 78% justify the isolation technique.

REFERENCES

Afraimovich, E. L., GPS global detection of the ionospheric response to solar flares, *Radio Sci. 35,* 1417-1424, 2000.

Bassiri, S. and G. A. Hajj, Higher-order ionospheric effects on the global positioning system observables and means of modeling them, *Manuscripta Geodaetica, 18,* 280-289, 1993.

Bomford, G., *Geodesy,* 4th ed., Oxford, New York, 1985.

Bracewell, R. N., *The Fourier Transform and Its Applications,* McGraw-Hill, New York, 1986.

Breiner, S., *Applications Manual for Portable Magnetometers,* Geometrics, San Jose, CA, 1973.

Constable, S., Constraints on mantle electrical conductivity from field and laboratory measurements, *J. Geomag. Geoelectr., 45,* 707-728, 1993.

Everett, M. E., personal communication, Department of Geology and Geophysics, Texas A&M University, 1999.

Everett, M. E., personal communication, Department of Geology and Geophysics, Texas A&M University, 2002.

Geometrics, *G-858 Magmapper 25309-OM REV.B Operations Manual,* San Jose, CA, 1995.

Hajj, G. and L. Romans, Ionospheric mapping with the GPS-MET, *Proceedings of the Institute of Navigation 52nd Annual Meeting*, Cambridge, MA, 539-545, 1996.

Hurn, J., *Differential GPS Explained,* Trimble, Sunnyvale, CA, 1993.

Jones, F. W. and A. T. Price, The geomagnetic effects of two-dimensional conductivity inhomogeneities at different depths, *Geophys. J. Roy. Ast. Soc., 22,* 333-345, 1971.

Kaufman, A. A., and G. V. Keller, *The Magnetotelluric Sounding Method,* Elsevier, New York, 1981.

Keller, G. V. and F. C. Fritschknect, *Electrical Methods in Geophysical Prospecting,* Pergamon, London, 1966.

Kivelson, M. G., and D. J. Southwood, Ionospheric traveling vortex generation by solar wind buffeting of the magnetopause, *J. Geophys. Res., 96,* 1661-1667, 1991.

Lizarralde, D., A. Chave, G. Hirth, and A. Shultz, Northeast Pacific mantle conductivity profile from long-period magnetotelluric sounding using Hawaii-to-California submarine cable data, *J. Geophys. Res., 100*, 17837-17854, 1995.

Lorrain, P. and D. R. Corson, *Electromagnetic Fields and Waves,* 2nd ed., Freeman, San Francisco, 1970.

McPherron, R. L., Magnetic pulsations: Their sources and relation to solar wind and geomagnetic activity*,* paper presented at the16th Electromagnetic Workshop, Santa Fe, NM, 2002.

National Geodetic Survey, GPS ephemerdes and pseudoranges, http://www.ngs.noaa.gov, 2003

National Geodetic Survey, GPS ephemerdes and pseudoranges, http://www.ngs.noaa.gov, 2004

National Geophysical Data Center, International Geomagnetic Reference Field 2000 (IGRF 2000) data, http://www.ngdc.noaa.gov, 2003.

National Geophysical Data Center, International Geomagnetic Reference Field 2000 (IGRF 2000) data, http://www.ngdc.noaa.gov, 2004.

Ramo, S., J. R. Whinnery, and T. Van Duzer, *Fields and Waves in Communication Electronics,* 2nd ed*.,* Wiley, New York, 1984.

Renfro, H. B., D. E. Feray, and P. B. King, *Geological Highway Map of Texas, H. B. Renfro Memorial Edition,* American Association of Petroleum Geology (AAPG), Tulsa, OK, 1973.

Robinson, E. A., *Multichannel Time Series Analysis With Digital Computer Programs,* 2nd ed*.,* Goose Pond, Houston, TX, 1983.

Seeber, G., *Satellite Geodesy,* De Gruyter, New York, 1993.

Sheriff, R. E., *Encyclopedic Dictionary of Exploration Geophysics*, 3rd. ed., Society of Exploration Geophysics, Tulsa, OK, 1991.

Snyder, J. P., *Map Projections—A Working Manual,* U. S. Geological Paper 1395, U. S. Government Printing Office, Washington, DC, 1987.

Spaulding, A. D.,Atmospheric noise and its effects of telecommunication system performance, in *Handbook of Atmospheric Electrodynamics,* vol. II*,* CRC Press, Boca Raton, FL, 1995.

Tarits, P. and N. Grammatica, Electromagnetic induction effects by the solar quiet magnetic field at satellite altitude, *Geophys Res. Lett., 27,* 4009-4012, 2000.

Telford, W. M., L. P. Geldart, R. E. Sheriff, and D. A. Keys, *Applied Geophysics,* Cambridge, New York, 1982.

Torge, W., *Geodesy,* DeGruyter, New York, 1991.

United States Geological Survey, *Chances Store,* 7.5' topographical map series, 1980. (Available at Sterling Evans Library, Texas A&M University.)

United States Geological Survey, *Crabapple,* 7.5' topographical map series, 1967. (Available at Sterling Evans Library, Texas A&M University.)

United States Geological Survey, *Enchanted Rock,* 7.5' topographical map series, 1967 (Available at Sterling Evans Library, Texas A&M University.)

United States Geological Survey, *National Atlas of the United States,* http://www.nationalatlas.gov, 2004

Von Seggern, D., *CRC Standard Curves and Surfaces,* CRC Press, Boca Raton, FL, 1993.

Vozoff, K., The magnetotelluric method in the exploration of sedimentary basins, *Geophysics, 37,* 98-141, 1972.

Ward, S. H. and G. W. Hohmann, Electromagnetic theory for geophysical applications, in *Electromagnetic Methods in Applied Geophysics,* vol. 1*,* edited by M. N. Nabighian , pp. 131-312, Society of Exploration Geophysicists, Tulsa, OK, 1994.

Weiss, C. J. and M. E. Everett, A three-dimensional B-spline model of upper mantle electrical conductivity via nonlinear c-response inversion, *Eos, Transactions, 77,* 46-168, 1996.

Worrall, D. M. and S. Snelson, Evolution of the northern Gulf of Mexico, with emphasis on Cenezoic growth faulting and the role of salt, in *The Geology of North America, Vol. A, The Geology of North America; An Overview,* edited by A. W. Bally and A. R. Palmer pp. 97-138, The Geological Society of America, Boulder, CO, 1989.

VITA

Eric Stephenson Erck

4414 Stanford Street
Chevy Chase, MD 20815

Education

● August 2004
Doctor of Philosophy, Geophysics, Texas A&M University, College Station, Texas
● May 1989
Master of Science, Geodesy and Photogrammetry, Iowa State University, Ames, Iowa: *Orthometric Height Difference Recovery Tests from GPS Observations and Gravimetry*
● May 1981
Bachelor of Science, Solid Earth Science, Purdue University, West Lafayette, Indiana

Professional Experience

● November 1990 – January 1993
Geodesist, Meridian Ocean Systems, San Jose, California and Houston, Texas
● July, 1989 – September, 1990
Senior Positioning Engineer, Geostar Corporation, Washington DC
● May, 1987 – May, 1989
Research Assistant, Iowa State University Department of Civil and Construction Engineering, Ames, IA
● April 1985 – July 1986
Exploration Geophysicist, Mobil Oil Corporation, Lafayette, Louisiana
● August 1981 – April 1985
Geophysicist, The Superior Oil Company, Houston, Texas

Publication

Elevation difference recovery tests from GPS observation and gravimetry, *Technical Papers, 1991 ACSM-ASPRS Annual Convention, Vol. 1,* 130-143, 1991 (Coauthor)